AIAA JOURNAL
Vol. 45, No. 4, April 2007

Finite Element Methods for Viscous Incompressible BiGlobal Instability Analysis on Unstructured Meshes

Leo M. González,[*] Vassilis Theofilis,[†] and Rafael Gómez-Blanco[‡]
Universidad Politécnica de Madrid, 28040 Madrid, Spain

DOI: 10.2514/1.25410

Viscous linear 3-D BiGlobal instability analyses of incompressible flows have been performed using finite element numerical methods, with a view to extend the scope of application of this analysis methodology to flows over complex geometries. The initial value problem (IVP), based on the linearized Navier–Stokes equations (LNSE), as well as the real and the complex partial-differential-equation-based generalized eigenvalue problems (EVP), have been solved. A mixed P_2P_1 finite element spatial discretization on unstructured meshes for both the LNSE and the EVP approaches has been used. For the time-discretization of the LNSE a characteristics method has been used for the first time in the context of flow stability analysis; the complex BiGlobal EVP has also been solved for the first time in the context of a finite element numerical discretization. In either its real or its complex form, the EVP has been solved without the need to introduce pseudocompressibility into the incompressible equations, which has simplified the systems to be solved without sacrificing accuracy. An Arnoldi approach has been used to recover the most significant eigenvalues. In this context, the associated solutions to the resulting linear systems were obtained by iterative methods: generalized minimal residual with incomplete lower–upper preconditioning or conjugate gradient with I-Cholesky preconditioning, depending on whether the coefficient matrix was symmetric or not. The 3-D instability of the classic 2-D lid-driven cavity flow and that of the rectangular duct flow were used as validation cases for the real and complex EVP, respectively. New results have been obtained for the 3-D BiGlobal instability of two closed and one open flow, namely, the regularized lid-driven cavity of rectangular and triangular shape and flow in the wake of a model bluff body.

Nomenclature

L_z = periodicity length in the Z direction
m = Krylov subspace dimension
N = number of quadratic (velocity) nodes
NL = number of linear (pressure) nodes
n = normal direction to the boundary
p = pressure
t = time
u_i = fluid velocity component
x_i = spatial coordinates $i = 1, 2, 3$; $x_1 = x$, $x_2 = y$, $x_3 = z$
β = wave number parameter, $2\pi/L_z$
Γ_D = Dirichlet boundary
Γ_N = outflow boundary
ε = parameter $\ll 1$
Ω = fluid domain
$\omega_i \equiv \Im\{\omega\}$ = perturbation frequency
$\omega_r \equiv \Re\{\omega\}$ = amplification/damping rate of linear perturbations

Superscripts

$-$ = basic flow component
$\wedge$ = amplitude function
$\sim$ = perturbation component

I. Introduction

LINEAR stability analysis of fluid flows has been used successfully for over one and a half centuries to elucidate phenomena originating from exponential growth of infinitesimal disturbances. The eigenvalue problem (EVP) that results from decomposition of flow quantities into basic and perturbation states has been used for most of the related analyses. In the last 15 years, modal EVP-based analyses have been complemented by nonmodal linear analyses, based on solutions of the associated initial value problem (IVP). In the limit of large times the IVP approach delivers results identical with those yielded by the EVP. However, several examples of shear flows exist for which solution of the IVP at early times delivers physically realistic predictions that are inaccessible to the EVP. As a consequence, linear stability analysis of a new flow problem should consider both methodologies.

Mathematical feasibility and computing efficiency has confined the bulk of linear stability analyses into the realm of one- or quasi-two-dimensional basic states; the first are commonly referred to as "parallel" flows. A review of classic theory, based on the linear eigenvalue problem as well as more modern developments in linear stability, associated with transient growth of linear disturbances that are exponentially damped in the limit of large times, may be found in the monographs by Drazin and Reid [1] and Schmid and Henningson [2]; both works are concerned with parallel flows.

The study of linear stability of 2-D, essentially nonparallel basic states, referred to as BiGlobal instability analysis [3], is also relatively recent. The origins of instability analyses of 2-D basic flows may be traced back to the works of Luijkx and Platten [4], who addressed convection in a rectangular channel, and those of Jackson [5], Zebib [6], and Morzynski and Thiele [7], who solved the 2-D BiGlobal instability of flow around a circular cylinder. Some connections of known parallel-flow instability results with those delivered by application of BiGlobal theory have recently appeared in the literature, in the case of instability of the incompressible zero- [8] or adverse- [9] pressure-gradient flat-plate boundary-layer flow. TriGlobal instability analysis results, pertaining to 3-D basic states,

---

Received 24 May 2006; revision received 5 October 2006; accepted for publication 5 October 2006.

[*] School of Naval Arquitecture, Avenida Arco de la Victoria s/n; previously Escuela Técnica Superior de Ingeniería (ICAI), Universidad Ponticia de Comillas, Alberto Aguilera 25, E-28015 Madrid, Spain.

[†] Corresponding Author, School of Aeronautics, Plaza Cardenal Cisneros 3; vassilis@aero.upm.es.

[‡] School of Aeronautics, Plaza Cardenal Cisneros 3; also Centro Logistico de Armamento y Experimentación (CLAEX), Ejercito del Aire, Torrejón de Ardoz Air Force Base, Spain.

have been presented by Gelfgat [10] on Rayleigh–Benárd convection and by Leriche and Labrosse [11] on Stokes eigenmodes in 3-D rectangular domains. It should be noted that nonmodal linear analyses may be treated by an eigenvalue problem approach when the entire spectrum is known [2]. Alternatively, one can solve the IVP; to-date a single analysis by Abdessemed et al. [12] is known to us, which deals with nonmodal linear instability of an essentially nonparallel flow, that around a low-pressure turbine cascade. On the other hand, the issue of absolute/convective instability in the context of a complex geometry may be dealt with using the impulse response and an IVP approach employing a linearized Navier–Stokes methodology [13].

Turning to numerical methods employed to analyze stability of nonparallel flows over complex geometries, it is interesting to note that a finite element spatial discretization has been used in the early BiGlobal analyses of Jackson [5] and Morzynski and Thiele [7]. Indeed, Li and Kot [14] had already applied finite element methods and Hermitian interpolation to analyze the stability of the (parallel) Poiseuille profile. Besides finite element methods, spectral methods have also been employed in BiGlobal linear stability theory. Noteworthy in this context is the work of Tatsumi and Yoshimura [15], who solved the 3-D global instability of flow in a rectangular duct. The high-resolution properties of spectral methods, permitting recovery of most accurate results from a necessarily limited number of nodes discretizing the PDE-based BiGlobal eigenvalue problem, has resulted in proliferation of these methods in current stability analyses of multidimensional basic states: see Theofilis [3] for a recent review.

The flexibility of the finite element approach was combined with the accuracy of the spectral method in the work of Barkley and Henderson [16], who employed the spectral element method [17] to solve 3-D instability of the periodic wake of the circular cylinder. In this work the complexity of the geometry was dealt with by patching regular subdomains/elements together. On the other hand, the first viscous BiGlobal instability analysis that used spectral elements in combination with an unstructured grid has been the work of Theofilis et al. [18] and those of Abdessemed et al. [12,19], who studied 3-D BiGlobal instability of flow over a NACA-0012 airfoil at an angle of attack and in a low-pressure turbine cascade, respectively.

In the context of both BiGlobal EVP and especially IVP solutions, there is a pressing need for further development and adaptation of numerical methods capable of solving complex flow instability problems, whereby complexity may refer to either Newtonian fluid flow over complex geometry or non-Newtonian fluid flow instability in regular geometries. One aspect of the present paper is a contribution toward satisfaction of the first need; see also the book of Karniadakis and Sherwin [17] with respect to the use of high-order spectral element methods on unstructured meshes for EVP-based BiGlobal instability analysis and the paper of Sherwin and Blackburn [20] who presented the first pulsatile flow BiGlobal instability analysis, also using high-order spectral element methods. Worth mentioning in the context of complex fluid flow instability is the work of Fietier and Deville [21], who performed the first BiGlobal instability of viscoelastic flows, also by a spectral element method.

By comparison, less work has been done in the area of global instability analysis using standard (low-order) finite element methods. Morzynski and coworkers have used such methods to unravel 2-D BiGlobal instability mechanisms in the wake of the cylinder. In a flow control context, they have demonstrated that the placement of a Strykowski [22] wire in the wake of a cylinder may be determined by solution of the 2-D BiGlobal eigenvalue problem, in which the flowfield around the main and the control cylinders is resolved by a finite element method. Furthermore, recent advances in flow control [23], in which BiGlobal instability analysis forms an essential part of the strategy for control of flow in the 2-D wake of a cylinder, were also based on finite element solutions of the associated EVPs. Finally, the first 3-D viscous BiGlobal instability analysis, employing finite elements and a pseudocompressibility method to solve the real EVP has been presented in a series of papers by Ding and Kawahara [24,25] on the instability of the classic lid-driven cavity.

The distinction between the real and the complex EVP is mandatory in the context of BiGlobal analysis. The large memory requirements for the numerical solution of a PDE-based EVP suggest that the appropriate form of the discretized linear operator be used: real, if the wave number vector is normal to the plane on which the basic flow develops and complex, if there is a basic flow velocity component parallel to the wave number vector [3]. It is only in the latter case that the doubling of the memory requirements for the discretization of the linear operator, compared with the former case, may be justified. To date no finite-element-based solution of the complex BiGlobal instability analysis EVP exists in the literature, and this is a second gap that the present contribution intends to fill.

The paper revisits by finite element methods earlier BiGlobal instability analyses in the context of both the linearized Navier–Stokes equations (LNSE) and the EVP and addresses previously inaccessible flow instability problems. The focus is mainly on numerical aspects, although new results of physical significance are presented in three out of the four configurations solved herein. Initially, the instability analysis of Tatsumi and Yoshimura [15] in the classic rectangular duct flow is revisited (for the first time) by the present method. Here, the EVP formulation results in a complex array, and no reduction to a real EVP is possible. Subsequently, closed and open flows are treated, the 2-D basic states of which have velocity components lying entirely on the plane normal to the wave number vector. Specifically, the BiGlobal instability of the regularized lid-driven cavity flow of rectangular [26] or triangular cross section, and that in the trailing edge of a model bluff body is analyzed. In all three cases the resulting LNSE and EVP formulations involve real arrays and the solutions are either real or complex conjugates [3]; the 3-D superposition of such linear disturbances on the basic flow is a standing wave pattern.

For the numerical solution of these problems, techniques are exposed that use the same finite element spatial discretization, the subspace of which satisfies the Ladysenskaja-Babuska-Brezzi (LBB) (or *inf-sup*) condition [27]. In the context of LNSE solutions, the characteristics method [28] is employed for the first time to this stability analysis problem. In the context of EVP solutions, available finite element approaches employ either or all of three techniques: a pseudocompressibility approach [24], a shift technique [29], or Cayley transforms [7,30]. The approach followed herein differs from previous works in that it uses the linearized equations of motion without the addition of pseudocompressibility or a Cayley transform, which results in a simple, yet efficient and accurate algorithm. Essential for the success of the analyses presented herein is the efficient iterative solution (using appropriate library software) of the large linear systems that result in either the LNSE or the EVP context.

After a presentation of the essential mathematical formulation in Sec. II (leaving some of the technical details for the Appendix), the suite of techniques developed is validated in Sec. III against known complex-EVP-based BiGlobal instability analyses in the rectangular duct [15] and real-EVP-based BiGlobal instability analysis results in the (singular) square lid-driven cavity [31]. Numerical experimentations are performed using the more demanding complex EVP on which the efficiency of the present method is assessed. Subsequently, the stability of two closed flows, the regularized lid-driven cavity of rectangular (including square) and equilateral triangular shape, is analyzed using both of the LNSE and the EVP approaches. Because of the geometric complexity of the triangular cavity problem, to date no attention has been paid to its linear instability and the present results are the first to identify the critical Reynolds number for amplification of 3-D disturbances superimposed upon the (typically solved in the literature) 2-D basic flow problem. Subsequently, 3-D BiGlobal instability in an open flow is studied, namely, flow in the wake of a bluff body, modeling the trailing edge of wings and turbine blades. Here motivation is provided by the recent intriguing results [32] regarding stabilization of the unsteady (Kármán) vortex street by means of modifying the wall boundary condition. Additional motivation is provided by the ongoing work on stability of low-pressure turbine flows (Abdessemed et al. [12,19]), especially in terms of potential modifications of the instability characteristics of the flow on account of imposition of periodic boundary conditions (appropriate in a turbine-blade cascade) as opposed to conditions of free development of the flow in the wake behind a bluff body. Concluding remarks are offered in Sec. IV.

II. Mathematical Formulation

The equations governing incompressible flows are written in primitive-variables formulation as follows:

$$\frac{\mathrm{D}u_i}{\mathrm{D}t} = -\frac{\partial p}{\partial x_i} + \frac{1}{Re}\frac{\partial^2 u_i}{\partial x_j^2} \quad \text{in } \Omega \tag{1}$$

$$\frac{\partial u_i}{\partial x_i} = 0 \quad \text{in } \Omega \tag{2}$$

$$u_i = f \quad \text{on } \Gamma_D \tag{3}$$

$$-pn_i + \frac{1}{Re}\frac{\partial u_i}{\partial n} = 0 \quad \text{on } \Gamma_N \tag{4}$$

Here Ω is the computational domain, Γ_D is the part of its boundary where Dirichlet boundary conditions are imposed, Γ_N is the part of the boundary where the "natural" boundary conditions (4) are imposed, n is the vector normal to the boundary Γ_N, the material derivative operator is defined as usual, $\frac{\mathrm{D}}{\mathrm{D}t} = \frac{\partial}{\partial t} + u_j\frac{\partial}{\partial x_j}$, and repeated indices imply summation.

A. Steady Laminar Basic Flows

The 2-D equations of motion are solved in the laminar regime at appropriate Reynolds number regions to compute steady basic flows $(\bar{u}_i, \bar{p})$ whose stability will subsequently be investigated. The equations read

$$\frac{\mathrm{D}\bar{u}_i}{\mathrm{D}t} = -\frac{\partial \bar{p}}{\partial x_i} + \frac{1}{Re}\frac{\partial^2 \bar{u}_i}{\partial x_j^2} \quad \text{in } \Omega \tag{5}$$

$$\frac{\partial \bar{u}_i}{\partial x_i} = 0 \quad \text{in } \Omega \tag{6}$$

$$\bar{u}_i = f \quad \text{on } \Gamma_D \tag{7}$$

$$-\bar{p}n + \frac{1}{Re}\frac{\partial \bar{u}_i}{\partial n} = 0 \quad \text{on } \Gamma_N \tag{8}$$

In three of the problems solved in what follows, the basic flow velocity vector is $(\bar{u}_1, \bar{u}_2, 0)^T$, that is, its component along the spatial direction x_3 is taken to be $\bar{u}_3 = 0$, and all components are taken to be independent of this spatial direction, $\frac{\partial \bar{u}_i}{\partial x_3} = 0$. The consequence is that the linearized equations of motion defining the BiGlobal stability problem to be solved may be expressed by real operators, as will be discussed shortly. In these three cases the basic flow is obtained by time integration of the system (5) and (6) by a semi-Lagrangian solver, starting from rest and being driven by the boundary conditions.

In the fourth problem analyzed, stability of constant-pressure-gradient-driven flow in a duct of rectangular cross section, the basic flow velocity vector is $(0, 0, \bar{u}_3)^T$, and is obtained by numerical solution of a Poisson problem, as discussed in the appropriate section.

B. Linear Systems

The basic flow is perturbed by small-amplitude velocity $\tilde{u}_i$ and kinematic pressure $\tilde{p}$ perturbations, as follows:

$$u_i = \bar{u}_i + \varepsilon\tilde{u}_i + c.c. \qquad p = \bar{p} + \varepsilon\tilde{p} + c.c. \tag{9}$$

where $\varepsilon \ll 1$ and $c.c.$ denote conjugate of the complex quantities $(\tilde{u}_i, \tilde{p})$. Substituting into Eqs. (1) and (2), subtracting the basic flow Eqs. (5) and (6), and linearizing, the equations for the perturbation quantities are obtained:

$$\frac{\bar{\mathrm{D}}\tilde{u}_i}{\mathrm{D}t} + \tilde{u}_j\frac{\partial \bar{u}_i}{\partial x_j} = -\frac{\partial \tilde{p}}{\partial x_i} + \frac{1}{Re}\frac{\partial^2 \tilde{u}_i}{\partial x_j^2} \tag{10}$$

$$\frac{\partial \tilde{u}_i}{\partial x_i} = 0 \tag{11}$$

with $\frac{\bar{\mathrm{D}}}{\mathrm{D}t} = \frac{\partial}{\partial t} + \bar{u}_j\frac{\partial}{\partial x_j}$. The boundary conditions used for this system are

$$\tilde{u}_i = 0 \quad \text{on } \Gamma_D \tag{12}$$

$$-\tilde{p}n_i + \frac{1}{Re}\frac{\partial \tilde{u}_i}{\partial n} = 0 \quad \text{on } \Gamma_N \tag{13}$$

The initial condition for (10) and (11) must be inhomogeneous for a nontrivial solution to be obtained. For the calculations presented, the following initial conditions have been used:

$$\tilde{u}_1(x, y, z; t = 0) = 1 \qquad \text{at the inflow boundary} \tag{14}$$

$$\tilde{u}_{2,3}(x, y, z; t = 0) = 0 \qquad \text{elsewhere} \tag{15}$$

In view of the spatial homogeneity along one spatial direction, $x_3 \equiv z$, the most general form assumed by the small-amplitude perturbations satisfies the following Ansatz:

$$\tilde{u}_i = \hat{u}_i(x, y, t)e^{i\beta z} \tag{16}$$

$$\tilde{p} = \hat{p}(x, y, t)e^{i\beta z} \tag{17}$$

where $i = \sqrt{-1}$, β is a wave number parameter, related with a periodicity length L_z along the homogeneous direction through $L_z = 2\pi/\beta$, and $(\hat{u}_i, \hat{p})$ are the complex amplitude functions of the linear perturbations. Note that the latter quantities may, at this stage, be arbitrary functions of time. Note also that in the case of the real EVP $(\hat{u}_i, \hat{p})$ may be real, pure imaginary, or pairs of complex conjugate solutions. Real and purely imaginary solutions also may appear in the case of stationary disturbances pertaining to the complex EVP. Traveling modes, in the latter case, are arbitrary complex functions.

1. *Linearized Navier–Stokes Equations and Solution Methodology*

In the absence of a basic flow velocity component along the spatial direction z, Eqs. (10) and (11) may be reformulated as

$$\frac{\bar{\mathrm{D}}\hat{u}_1}{\mathrm{D}t} + \hat{u}_j\frac{\partial \bar{u}_1}{\partial x_j} = -\frac{\partial \hat{p}}{\partial x} + \frac{1}{Re}\left(\frac{\partial^2}{\partial x_j^2} - \beta^2\right)\hat{u}_1 \tag{18}$$

$$\frac{\bar{\mathrm{D}}\hat{u}_2}{\mathrm{D}t} + \hat{u}_j\frac{\partial \bar{u}_2}{\partial x_j} = -\frac{\partial \hat{p}}{\partial y} + \frac{1}{Re}\left(\frac{\partial^2}{\partial x_j^2} - \beta^2\right)\hat{u}_2 \tag{19}$$

$$\frac{\bar{\mathrm{D}}\hat{u}_3}{\mathrm{D}t} = -i\beta\hat{p} + \frac{1}{Re}\left(\frac{\partial^2}{\partial x_j^2} - \beta^2\right)\hat{u}_3 \tag{20}$$

$$\frac{\partial \hat{u}_1}{\partial x} + \frac{\partial \hat{u}_2}{\partial y} + i\beta \hat{u}_3 = 0 \tag{21}$$

This system may be integrated along the characteristic lines from the feet of the characteristic line at time level t^{n^*} to the next time level t^{n+1} as follows:

$$\hat{u}_1^{n+1} = \hat{u}_1^{n^*} - \Delta t \hat{u}_j^{n^*} \frac{\partial \bar{u}_1}{\partial x_j} - \Delta t \frac{\partial \hat{p}^{n+1}}{\partial x} + \frac{\Delta t}{2Re}\left(\frac{\partial^2}{\partial x_j^2} - \beta^2\right) \times \left(\hat{u}_1^{n+1} + \hat{u}_1^{n^*}\right) \tag{22}$$

$$\hat{u}_2^{n+1} = \hat{u}_2^{n^*} - \Delta t \hat{u}_j^{n^*} \frac{\partial \bar{u}_2}{\partial x_j} - \Delta t \frac{\partial \hat{p}^{n+1}}{\partial y} + \frac{\Delta t}{2Re}\left(\frac{\partial^2}{\partial x_j^2} - \beta^2\right) \times \left(\hat{u}_2^{n+1} + \hat{u}_2^{n^*}\right) \tag{23}$$

$$\hat{u}_3^{n+1} = \hat{u}_3^{n^*} - i\Delta t \beta \hat{p}^{n+1} + \frac{\Delta t}{2Re}\left(\frac{\partial^2}{\partial x_j^2} - \beta^2\right)\left(\hat{u}_3^{n+1} + \hat{u}_3^{n^*}\right) \tag{24}$$

$$0 = \frac{\partial \hat{u}_1^{n+1}}{\partial x} + \frac{\partial \hat{u}_2^{n+1}}{\partial y} + i\beta \hat{u}_3^{n+1} \tag{25}$$

where $\hat{u}_i^{n^*}$ is the interpolated velocity at the feet of the characteristic at time t_n. The calculation of the feet of the characteristics is done by the finite element interpolation using a nonlinear equation involving the basis functions of the velocity. The method is applicable to both structured and unstructured grids, although an efficient search–locate algorithm is necessary for the solution of the nonlinear equation [28,33]. An explicit integration for the term $\hat{u}_j^{n^*} \frac{\partial \bar{u}_2}{\partial x_j}$ has been considered. Equations (22–25) may be written in compact form as

$$\mathcal{L}\,\hat{u}_1^{n+1} = \mathcal{R}\hat{u}_1^{n^*} - \Delta t\left(\hat{u}_j^{n^*} \frac{\partial \bar{u}_1}{\partial x_j} + \frac{\partial \hat{p}^{n+1}}{\partial x}\right) \tag{26}$$

$$\mathcal{L}\,\hat{u}_2^{n+1} = \mathcal{R}\hat{u}_2^{n^*} - \Delta t\left(\hat{u}_j^{n^*} \frac{\partial \bar{u}_2}{\partial x_j} + \frac{\partial \hat{p}^{n+1}}{\partial y}\right) \tag{27}$$

$$\mathcal{L}\,\hat{u}_3^{n+1} = \mathcal{R}\hat{u}_3^{n^*} - i\Delta t \beta \hat{p}^{n+1} \tag{28}$$

$$\frac{\partial \hat{u}_1^{n+1}}{\partial x} + \frac{\partial \hat{u}_2^{n+1}}{\partial y} + i\beta \hat{u}_3^{n+1} = 0 \tag{29}$$

where

$$\mathcal{L} = \left(1 + \frac{\Delta t \beta^2}{2Re} - \frac{\Delta t}{2Re}\frac{\partial^2}{\partial x_j^2}\right) \tag{30}$$

and

$$\mathcal{R} = \left(1 - \frac{\Delta t \beta^2}{2Re} + \frac{\Delta t}{2Re}\frac{\partial^2}{\partial x_j^2}\right) \tag{31}$$

are both symmetric operators. The boundary and initial conditions used for this system are (12–15), respectively. The spatial discretization of (26–29) is performed using mixed finite elements Taylor–Hood type. The mixed interpolation for the velocity and pressure eigenfunctions can be expressed as

$$\hat{u}_i = \psi_\alpha \hat{u}_i^\alpha \qquad (\alpha = 1, \ldots, N) \tag{32}$$

$$\hat{p} = \psi_\lambda \hat{p}^\lambda \qquad (\lambda = 1, \ldots, \mathrm{NL}) \tag{33}$$

where N and NL are the number of quadratic and linear nodes used for the discretization of the velocity and pressure, respectively. Using the method of characteristics for time integration [28,33], the LNSE problem represented by Eqs. (18–21) has been transformed into a Stokes problem, as defined by Dean and Glowinski [34]. A conjugate gradient algorithm [34] is well-suited for the solution of the Stokes problem obtained and has been used here; the symmetric structure of the $\mathcal{L}$ operator has also permitted the solution of all linear systems by a conjugate gradient algorithm [35].

2. *Eigenvalue Problem Formulation and Solution Methodology*

The separability of temporal and spatial derivatives in (10) and (11) permits introduction of an explicit harmonic temporal dependence of the disturbance quantities into these equations, according to the Ansatz:

$$\tilde{u}_i = \hat{u}_i(x, y) e^{i\beta z} e^{\omega t} \tag{34}$$

$$\tilde{p} = \hat{p}(x, y) e^{i\beta z} e^{\omega t} \tag{35}$$

where a temporal formulation has been adopted, considering β a real wave number parameter, whereas ω is the complex eigenvalue sought. Substitution into (10) and (11) results in

$$\left\{\bar{u}_j \frac{\partial}{\partial x_j} + \frac{\partial \bar{u}_1}{\partial x} + i\beta \bar{u}_3 - \frac{1}{Re}\left(\frac{\partial^2}{\partial x_j^2} - \beta^2\right)\right\}\hat{u}_1 + \hat{u}_2 \frac{\partial \bar{u}_1}{\partial y} + \frac{\partial \hat{p}}{\partial x} = -\omega \hat{u}_1 \tag{36}$$

$$\left\{\bar{u}_j \frac{\partial}{\partial x_j} + \frac{\partial \bar{u}_2}{\partial y} + i\beta \bar{u}_3 - \frac{1}{Re}\left(\frac{\partial^2}{\partial x_j^2} - \beta^2\right)\right\}\hat{u}_2 + \hat{u}_1 \frac{\partial \bar{u}_2}{\partial x} + \frac{\partial \hat{p}}{\partial y} = -\omega \hat{u}_2 \tag{37}$$

$$\left\{\bar{u}_j \frac{\partial}{\partial x_j} + i\beta \bar{u}_3 - \frac{1}{Re}\left(\frac{\partial^2}{\partial x_j^2} - \beta^2\right)\right\}\hat{u}_3 + \hat{u}_1 \frac{\partial \bar{u}_3}{\partial x} + \hat{u}_2 \frac{\partial \bar{u}_3}{\partial y} + i\beta \hat{p} = -\omega \hat{u}_3 \tag{38}$$

$$\frac{\partial \hat{u}_1}{\partial x} + \frac{\partial \hat{u}_2}{\partial y} + i\beta \hat{u}_3 = 0 \tag{39}$$

3. *Complex EVP*

In the presence of a basic flow velocity vector comprising components $(\bar{u}_1, \bar{u}_2, \bar{u}_3)^T$, one defines

$$\alpha_{ii} = \left\{\bar{u}_j \frac{\partial}{\partial x_j} + \frac{\partial \bar{u}_i}{\partial x_i} - \frac{1}{Re}\left(\frac{\partial^2}{\partial x_j^2} - \beta^2\right) + i\beta \bar{u}_3\right\}, \qquad j = 1, 2 \tag{40}$$

where no Einstein summation on the index i is implied. The complex nonsymmetric operator A is defined by

$$A = \begin{pmatrix} \alpha_{11} & \frac{\partial \bar{u}_1}{\partial y} & 0 & \frac{\partial}{\partial x} \\ \frac{\partial \bar{u}_2}{\partial x} & \alpha_{22} & 0 & \frac{\partial}{\partial y} \\ \frac{\partial \bar{u}_3}{\partial x} & \frac{\partial \bar{u}_3}{\partial y} & \alpha_{33} & i\beta \\ \frac{\partial}{\partial x} & \frac{\partial}{\partial y} & i\beta & 0 \end{pmatrix} \tag{41}$$

After the variational formulation, details of which are presented in the Appendix, the operator A, which is represented by a $(3N + \mathrm{NL})^2$ matrix, becomes

$$A = \begin{pmatrix} F_{ij} + C_{ij}^{11} + i\beta E_{ij} & C_{ij}^{12} & 0 & -\lambda_{ij}^{x} \\ C_{ij}^{21} & F_{ij} + C_{ij}^{22} + i\beta E_{ij} & 0 & -\lambda_{ij}^{y} \\ C_{ij}^{31} & C_{j}^{32} & F_{ij} + i\beta E_{ij} & i\beta D_{ij} \\ \lambda_{ji}^{x} & \lambda_{ji}^{y} & i\beta D_{ji} & 0 \end{pmatrix} \tag{42}$$

where $F_{ij} \equiv \gamma_{ij} + (R_{ij} + \beta^2 M_{ij})$. The real symmetric operator B is also introduced by

$$B = \begin{pmatrix} M_{ij} & 0 & 0 & 0 \\ 0 & M_{ij} & 0 & 0 \\ 0 & 0 & M_{ij} & 0 \\ 0 & 0 & 0 & 0 \end{pmatrix}, \qquad i, j = 1, \cdots, N \tag{43}$$

where M represents the mass matrix; the elements of all matrices introduced in (42) and (43) are presented in the Appendix. The system (36–39) is thus transformed into the (complex) generalized eigenvalue problem for the determination of ω:

$$A \begin{pmatrix} \hat{u}_1 \\ \hat{u}_2 \\ \hat{u}_3 \\ \hat{p} \end{pmatrix} = -\omega B \begin{pmatrix} \hat{u}_1 \\ \hat{u}_2 \\ \hat{u}_3 \\ \hat{p} \end{pmatrix} \tag{44}$$

The complex generalized eigenvalue problem (44) has either real or complex solutions, corresponding to stationary ($\omega_i = 0$) or traveling ($\omega_i \neq 0$) modes.

4. *Real EVP*

In the case of a basic flow velocity vector with components $(\bar{u}_1, \bar{u}_2, 0)^T$ only on the plane normal to the wave number vector, it is possible to deduce a real eigenvalue problem, by the redefinition of the out-of-plane velocity component [3]:

$$\hat{u}_{\,3} \equiv i\hat{u}_3$$

This converts the system (36–39) into one with real coefficients. Defining

$$\alpha_{ii} = \left\{ \bar{u}_j \frac{\partial}{\partial x_j} + \frac{\partial \bar{u}_i}{\partial x_i} - \frac{1}{Re}\left(\frac{\partial^2}{\partial x_j^2} - \beta^2 \right) \right\}, \qquad j = 1, 2 \tag{45}$$

(no Einstein summation implied for index i), the left-hand side of the system can be represented by the real nonsymmetric operator A as

$$A = \begin{pmatrix} \alpha_{11} & \frac{\partial \bar{u}_1}{\partial y} & 0 & \frac{\partial}{\partial x} \\ \frac{\partial \bar{u}_2}{\partial x} & \alpha_{22} & 0 & \frac{\partial}{\partial y} \\ 0 & 0 & \alpha_{33} & -\beta \\ \frac{\partial}{\partial x} & \frac{\partial}{\partial y} & \beta & 0 \end{pmatrix} \tag{46}$$

After the variational formulation, details of which are presented in the Appendix, the real operator A becomes

$$A = \begin{pmatrix} F_{ij} + C_{ij}^{11} & C_{ij}^{12} & 0 & -\lambda_{ij}^{x} \\ C_{ij}^{21} & F_{ij} + C_{ij}^{22} & 0 & -\lambda_{ij}^{y} \\ 0 & 0 & F_{ij} & -\beta D_{ij} \\ \lambda_{ji}^{x} & \lambda_{ji}^{y} & \beta D_{ji} & 0 \end{pmatrix} \qquad i, j = 1, \cdots 4 \tag{47}$$

The generalized eigenvalue problem is again defined as in (44) but is now real, with B the same symmetric real operator and A defined by (46). Because the operators A and B are real in this subclass of problems, the generalized eigenvalue problem (44) has either real or complex conjugate pairs of solutions. On the other hand, real arithmetic suffices for the calculation and storage of (and subsequent operations with) the nonzero elements of the matrices A and B.

5. *Krylov Subspace Iteration*

From a linear stability analysis point of view, the most important eigenvalues are those closest to the axis $\omega_r = 0$ and here an iterative method has been used for their determination. Specifically, the well-established in BiGlobal linear instability problems [3] Arnoldi algorithm has been used.

The Arnoldi method is a subspace iteration method, the computation time of which depends linearly on the subspace dimension. As experienced in earlier analogous studies [24] only eigenvalues with large modules can be obtained by straightforward application of the algorithm. Because the eigenvalues closest to the imaginary axis are sought, a simple transformation is used to convert the original problem into one where the desired values have large modules. Note that the eigenvectors are not affected by this transformation. Specifically, defining

$$\mu = -\omega^{-1} \tag{48}$$

and

$$\Phi = \begin{pmatrix} \hat{u}_1 \\ \hat{u}_2 \\ \hat{u}_3 \\ \hat{p} \end{pmatrix} \tag{49}$$

it follows that

$$A^{-1} B \Phi = \mu \Phi, \qquad A^{-1} B = C, \qquad C\Phi = \mu\Phi \tag{50}$$

This transformation converts the original generalized into the standard EVP. A finite but small (compared with the leading dimension of A, B) number of eigenvalues (equal to the Krylov subspace dimension) m is sought, which is obtained by application of the Arnoldi algorithm as follows:

```
1) CHOOSE an initial random vector $v_1$ and NORMALIZE it.
2) FOR $j = 1, 2, \ldots m$ DO:
    a) Calculate $w_j$ as $Cv_j = w_j$, which is equivalent to solve the problem $Aw_j = Bv_j$ ($A$ nonsymmetric).
    b) FOR $i = 1, 2, \ldots j$ DO:
        $h_{ij} = (Cv_j, v_i)$    (51)
        $a = \sum_{i=1}^{j} h_{ij} v_i$    (52)
        $\hat{v}_{\,j+1} = w_j - a$    (53)
        $h_{j+1,j} = \|\hat{v}_{j+1}\|$    (54)
        $v_{j+1} = \frac{\hat{v}_{j+1}}{h_{j+1,j}}$    (55)
    END DO
END DO
```

This algorithm delivers an orthonormal basis $\boldsymbol{V}_m = [v_1, v_2, \ldots, v_m]$ of the Krylov subspace $\boldsymbol{K}_m = \mathrm{span}\{v_1, Cv_1, \ldots, C^{m-1}v_1\}$. The restriction from $\boldsymbol{C}$ to $\boldsymbol{K}_m$ is represented by the matrix $\boldsymbol{H}_m = \{h_{ij}\}$. The eigenvalues of the latter matrix are an approximation of the m largest eigenvalues of the original problem (44). The eigenvectors associated with these eigenvalues may be obtained from

$$\Phi_i = \boldsymbol{V}_m \tilde{y}_i \tag{56}$$

where $\tilde{y}_i$ is an eigenvector of $\boldsymbol{H}_m$ associated with the μ_ith eigenvalue.

Note that, because the matrix C is unknown a priori, a nonsymmetric linear system $Cv_j = A^{-1}Bv_j = q_j$ or, equivalently, $Aq_j = Bv_j$ must be solved at each iteration, q_j being an unknown auxiliary vector. Such linear systems have been solved by a direct method by Ding and Kawahara [24] in the context of finite element and by Theofilis et al. [36] in the context of spectral methods.

6. *Numerical Considerations*

The leading dimension of the matrices resulting from the finite element discretization is taken to be substantially larger than that typically used in spectral BiGlobal instability analyses, as a consequence of the fine resolutions required to compensate for the low order of the numerical scheme. Hence, the solution of these large linear systems with a nonsymmetric matrix A is performed using an iterative generalized minimal residual (GMRES) algorithm with incomplete lower–upper (ILU) preconditioning appropriate for sparse systems.

All computations have been performed *serially* on a 3.0 GHz Intel P-IV PC. A typical leading dimension of matrix A used in the present analyses is $\mathrm{DIM}(A) \equiv 3N + \mathrm{NL} = \mathcal{O}(7 \times 10^4)$, whereas only the nonzero elements of this matrix, $\mathcal{O}(9 \times 10^6)$, and those of its ILU decomposition, $\mathcal{O}(10^8)$, are stored. The basic GMRES and ILU codes of the Sparsekit [37] library were modified to adapt them to the problem at hand. Incidentally, it is worth mentioning that one of the issues encountered in the ILU decomposition process is to obtain estimates of the dimension of the ILU preconditioner before calculating it; this dimension depends on the tolerance chosen for the preconditioner. The efficiency of linear solver depends on the following items:

1) *Coefficient matrix A*. This, in turn, depends on the Reynolds number, β, and the mesh used. The size of this sparse matrix increases with the total mesh nodes. For a fixed grid, changes in Reynolds number and β result in changes in the condition number of the matrix. Consequently, the need for a preconditioner will be more or less acute, depending largely on the value of the Reynolds number considered; the larger the Reynolds number, the stronger the need to precondition the linear systems.

2) *ILU Preconditioner*. It is inconceivable to solve the linear systems arising in this type of analysis without preconditioning. This results in the need to generate an ILU matrix, which depends on a tolerance parameter (t-ILU); this parameter sets the threshold for dropping small terms in the factorization. If t-ILU is set too low, a good preconditioner results, but its size can be unmanageable for serial computations of the kind considered presently. On the other hand, if t-ILU is set too high, the preconditioner will be easily allocated in PC-class memories but its quality may be poor, such that the resulting number of iterations may grow out of control. As a consequence, the number of nonzero elements of the preconditioner depend on t-ILU and is not known in advance of the computation. An estimated size for the preconditioner must be provided before running the Arnoldi algorithm; if the result is not satisfactory, two remedies are possible: if sufficient memory is available the size of the preconditioner may be increased, keeping t-ILU constant; if the limit of the available memory has been reached, t-ILU should be decreased until the preconditioner fits into the estimated size.

3) *Solver tolerance* (t-GMRES). This is the tolerance used as a stopping criterion in the iterative process. This is stopped as soon as the Euclidean norm of the current residual divided by the Euclidean norm of initial residual becomes less than t-GMRES.

The total time needed for a complete Arnoldi analysis depends mostly on the efficiency of the linear solver as already described, as well as on the Krylov space dimension m used to approximate the most important eigenvalues. A concrete example will be discussed in the (most expensive) problem of linear instability of rectangular duct flow.

III. Results

All analyses presented in what follows concern steady basic states. The existence of a steady 2-D basic state implies its stability with respect to 2-D ($\beta = 0$) perturbations and the objective of the analysis is the interrogation of this state with respect to its stability to 3-D ($\beta \neq 0$) disturbances. In this context, it is interesting to allude to the issue of computation of an unstable basic flow (corresponding to an unstable $\beta = 0$ perturbation): such basic states are typically obtained by continuation methods and Newton iteration to follow the flow from the left (stable) into the right (unstable) half-plane; no such unsteady flow has been analyzed here. Another class of unsteady flows not treated presently is that of time-periodic states, the stability of which may be analyzed using Floquet theory [12,16]. The development and validation on steady basic states of the finite element tools described earlier is the first step toward future development of tools capable of analyzing both aforementioned classes of unsteady flows.

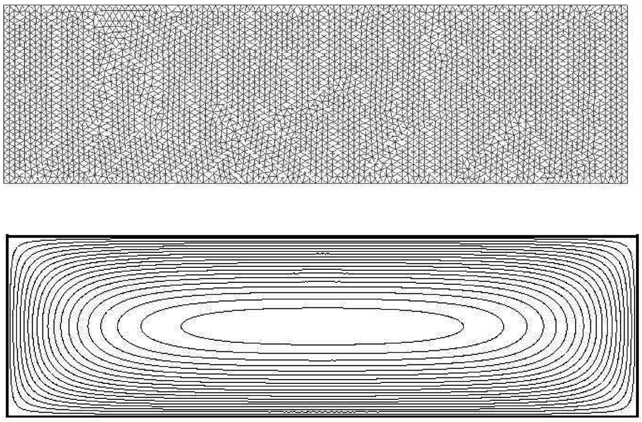

Fig. 1 Unstructured grid comprising 1.3 x 10^4 nodes (upper) and basic flow velocity component $\bar{w}(x,y)$ (lower) of flow in an AR = 3.5 rectangular duct. Shown are 14 isolines between 0 and 0.99151.

A. Basic flows

1. *Rectangular Duct Flow*

The first application studied is the pressure-gradient-driven flow in a rectangular duct. The linear instability of this problem, introduced in the seminal work of Tatsumi and Yoshimura [15], is now well understood [36,38,39]. Interesting, in the present context, is the fact that no finite element solutions of this BiGlobal EVP are known in the literature, and it is desirable to establish the capacity of the methods described herein to address this problem, as well as identify their potential limitations.

The single component of the basic flow velocity vector, $(0, 0, \bar{w})^T$,[§] is obtained from numerical solution (using a straightforward GMRES algorithm) of the Poisson problem:

$$\partial_{xx}\bar{w}(x, y) + \partial_{yy}\bar{w}(x, y) = -2 \tag{57}$$

$$\bar{w}(x, y)|_{\Gamma_b} = 0 \tag{58}$$

using the same $P2P1$ numerical discretization as subsequently used for the solution of the EVP. The unstructured grid used and the solution obtained at aspect ratio AR = 3.5 are presented in Fig. 1.

2. *Rectangular Regularized Lid-Driven Cavity*

A rectangular lid-driven cavity domain $x \in [0, \mathrm{AR}] \times y \in [0, 1]$ is defined, AR being the cavity aspect ratio. Flow is driven by the motion of the lid placed at $y = 1$ along the positive x direction, which results in a two-component basic velocity vector, $(\bar{u}, \bar{v}, 0)^T$. The lid velocity is regularized according to Bourcier and Francois [26]:

$$\bar{u} = Kx^2(AR - x)^2 \quad \text{at } y = 1 \tag{59}$$

whereas $\bar{u} = 0$ on the other three and $\bar{v} = 0$ on all four cavity

---

[§] The notation $(\bar{u}_1, \bar{u}_2, \bar{u}_3)^T \equiv (\bar{u}, \bar{v}, \bar{w})^T$ and $(\hat{u}_1, \hat{u}_2, \hat{u}_3)^T \equiv (\hat{u}, \hat{v}, \hat{w})^T$ has been used interchangeably in what follows.

Table 1 Convergence study for the steady basic flow in a square cavity at $Re = 200$

No. of nodes	$\max\{\bar{p}\} - \min\{\bar{p}\}$	$\min\{\bar{u}(x = 0.5, y)\}$	$\max\{\bar{v}(x, y = 0.5)\}$	$\min\{\bar{v}(x, y = 0.5)\}$
5129	0.3217	−0.26226	0.2483	−0.35739
11,525	0.3452	−0.25128	0.2314	−0.34907
20,689	0.4116	−0.18784	0.16366	−0.25689
32,153	0.4115	−0.18801	0.16373	−0.25743

boundaries. The constant K depends on the aspect ratio of the cavity and is calculated such that $\bar{u}(x = \mathrm{AR}/2, y = 1) = 1.0$. Other regularization possibilities exist, notably the well-tested approximation of the singular lid-driven cavity presented by Leriche et al. [40], but have not been used here. It is worth noting that regularization of the boundary conditions in the cavity problem is essential to obtain a well-posed problem and avoid having to enter into the somewhat artificial debate found in the literature on the critical conditions for instability (cf. Poliashenko and Aidun [41] and related subsequent work) of a singular basic flow.

To ensure spatial convergence, an unstructured mesh of uniform-sized equilateral triangular elements having a side of size 0.015 (scaled on the cavity depth) has been used, after some numerical experimentation. This results in $N = 20,689$ (quadratic) velocity nodes and $\mathrm{NL} = 5012$ (linear) pressure nodes; the results obtained have been confirmed by higher-resolution computations using $\mathcal{O}(3 \times 10^4)$ velocity nodes: Table 1 summarizes grid converge studies. Note also that, as mentioned, such a mesh is substantially finer than those used by Ding and Kawahara [24] or Theofilis et al. [36] in the related (singular) lid-driven cavity problem.

With respect to convergence in time, the relative tolerance

$$\mathrm{tol} \equiv \max_i \{|f_i(t + \Delta t) - f_i(t)|\} < 10^{-15} \tag{60}$$

has been used, where f_i is the local value in a node i of any flow quantity. The time step used for this calculations was 0.01 nondimensional time units, which resulted in well-acceptable total running times. Basic flow results at $Re = 200$ are presented in Fig. 2.

3. *Triangular Regularized Lid-Driven Cavity*

Whereas the rectangular cavity application was chosen to complete earlier work using spectral methods [31], the triangular geometry is ideally suited for the triangular-element-based unstructured mesh calculations, such that the flexibility of the present numerical approach can be put to optimal use in the much less-studied flow in the triangular geometry. Basic flows using the singular boundary conditions are discussed extensively by Erturk and Gokol [42] and references therein [43–45]. Only the equilateral triangle geometry has been considered presently; of the different definitions of the triangle found in the literature, here the vertices are chosen at the points $(x = 0, y = 0)$, $(1, 0)$, and $(\frac{1}{2}, -\frac{\sqrt{3}}{2})$, such that the resulting triangle side is unity.

Flow is driven by the motion of the lid placed at $y = 0$ along the positive x direction. The lid velocity is regularized as in (59), taking $K = 2^4$; in addition, the boundary conditions $\bar{u} = 0$ on the other two and $\bar{v} = 0$ on all three cavity boundaries have been used in a time-accurate solution for the calculation of the basic state, according to the discussion of the preceding section.

Fine spatial resolution was ensured by use of an unstructured mesh comprising $\mathcal{O}(8 \times 10^4)$ (quadratic) velocity nodes, as shown in Fig. 3. Time step and basic flow time convergence criteria were used in line with those of the rectangular cavity. The converged values of the (spanwise) vorticity and those of the two velocity components at the barycenter of the triangle are shown in Table 2. It has to be noted that a resolution such as that used in the basic flow calculations was well feasible on the machine used.

4. *Wake of a Model Bluff Body*

The third real-EVP-based BiGlobal instability problem studied has been the wake of a bluff-body model, typically encountered in civil engineering applications. In two spatial dimensions the model consists of a rectangular body, the trailing edge of which has rounded corners of a curvature radius r, as schematically depicted in Fig. 4a. The characteristic length of the problem is the side of the square D (the width, in the case of a parallelogram), using which all lengths are nondimensionalized. Rotation is permitted at the downstream corners of the bluff body, as also shown in Fig. 4a. The parameters $\lambda_r = r/D$ and $A_r = \frac{V_r}{U_0}$, with U_0 and V_r the freestream and rotation velocities, respectively, fully describe the problem and are used as control parameters of the wake flow.

It has been demonstrated that it is possible to control flow in the wake by modifying the boundary condition in the neighborhood of the trailing edge. Patnaik and Wei [32] have used a boundary condition of $A_r \neq 0$ as a means of controlling the flow in the wake, and were able to obtain steady flows at conditions at which, under no rotation, the flow would be unsteady. The same 2-D direct numerical

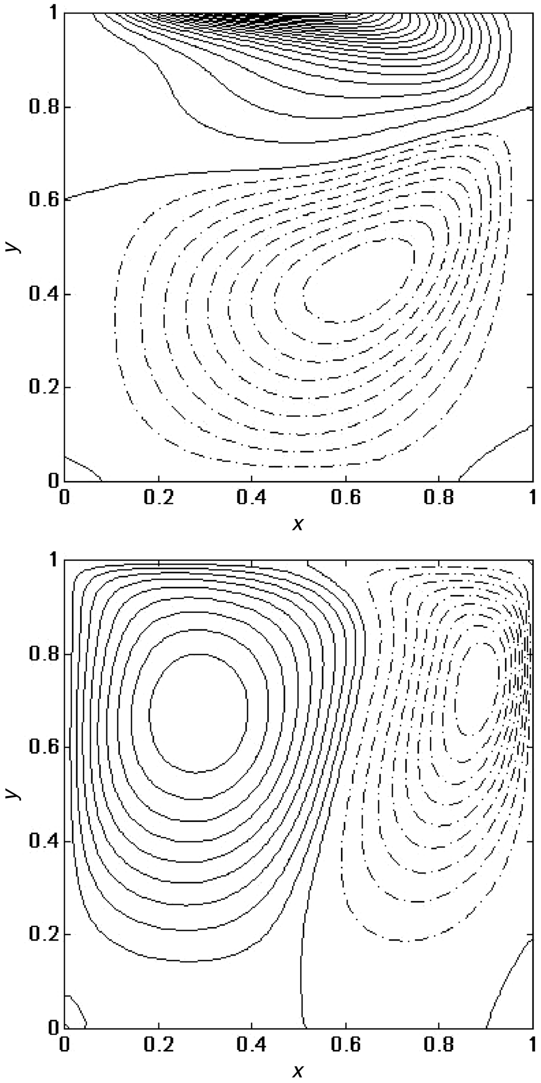

Fig. 2 $\bar{u}$ (upper) and $\bar{v}$ (lower) velocity components of the basic flow in the regularized cavity problem at $Re = 200$. Nine isolines between −0.2 and 0 and ten isolines between 0 and 1 are shown for $\bar{u}$, and 20 isolines between −0.35 and 0.15 are shown for $\bar{v}$.

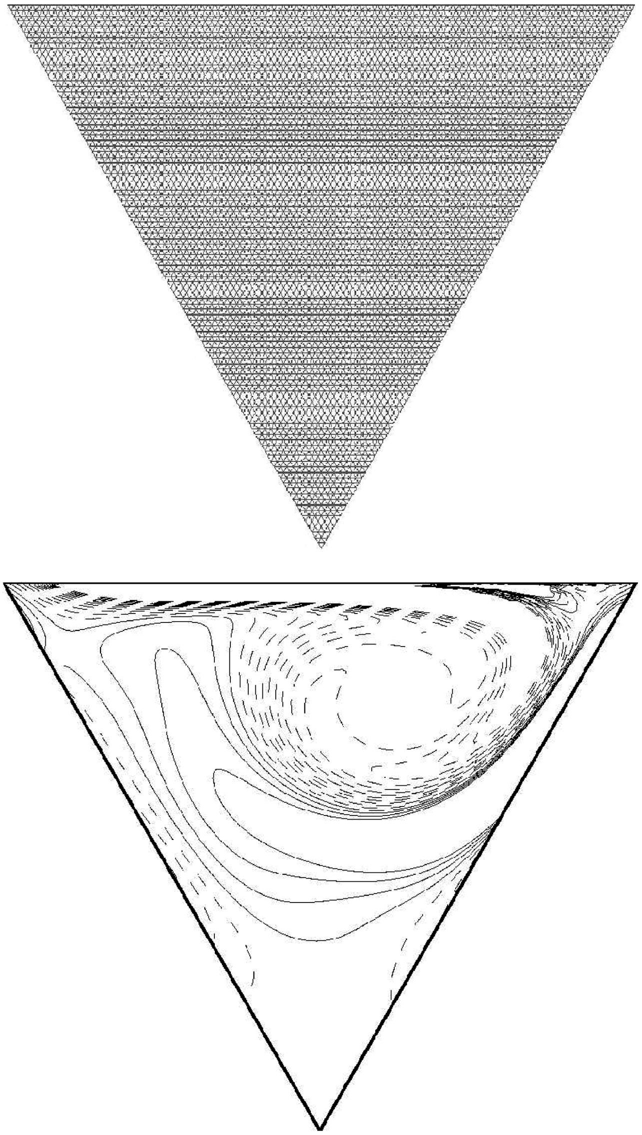

Fig. 3 Grid (upper) and basic flow vorticity component (lower) of flow in the triangular regularized cavity at $Re = 1870$. Shown are 14 isolines between -5 and 1.5.

simulation (DNS) solver used in the previous applications has also been employed here to calculate basic flows in both the square and the rectangular geometry. The boundary conditions considered have been a hyperbolic tangent streamwise velocity profile at the inflow boundary, Γ_{in}; no-slip at the body surface, Γ_b; natural boundary conditions for the outflow boundary Γ_{out}; and unit streamwise velocity, $(\bar{U}_0, \bar{v}) = (1, 0)$, at the upper and lower boundaries, Γ_{ul}. In the case studied the curvature radius of the rounded corners of the bluff body was fixed at $r = 0.4$. A mesh comprising 38,055 nodes and 18,656 elements has been used, a detail of which is shown in Fig. 4b. If $A_r = 0$ at this value of $r = 0.4$, unsteadiness has been identified to exist at $Re = \frac{U_0 D}{\nu} > 80$, where ν is the kinematic viscosity, as shown in Fig. 4c. On the other hand, a small amount of rotation, $A_r = 0.1$, results in a steady wake, shown in Fig. 4d, in line with the analogous result of Patnaik and Wei.

Table 2 Steady basic flow vorticity and velocity components at the barycenter ($x = 0.50, y = -0.28$) of the equilateral triangular lid-driven cavity flow

Re	$-\bar{u}_y + \bar{v}_x$	$\bar{u}$	$\bar{v}$
1800	-3.6886	-0.207835	0.12958
2100	-0.6227	-0.227509	0.17141
2400	1.0986	-0.189996	0.15120
2700	1.8654	-0.151705	0.12521
3000	2.1318	-0.117960	0.10055

From a physical point of view, in the present BiGlobal instability analysis context, an assertion of Patnaik and Wei [32] is of interest, which associates the stabilization of the wake with the existence of regions of absolute and convective instability in the wake. Here, attention is only paid on the numerical aspects of the BiGlobal EVP solution, whereas results from a physical point of view will be presented elsewhere. A key difference with the flows studied earlier is that the wake flow is an open system and it is interesting to verify the performance and identify the limits of the present finite element methodology in this class of problems. In particular the performance of the boundary conditions for an open flow problem has been monitored, as described in what follows.

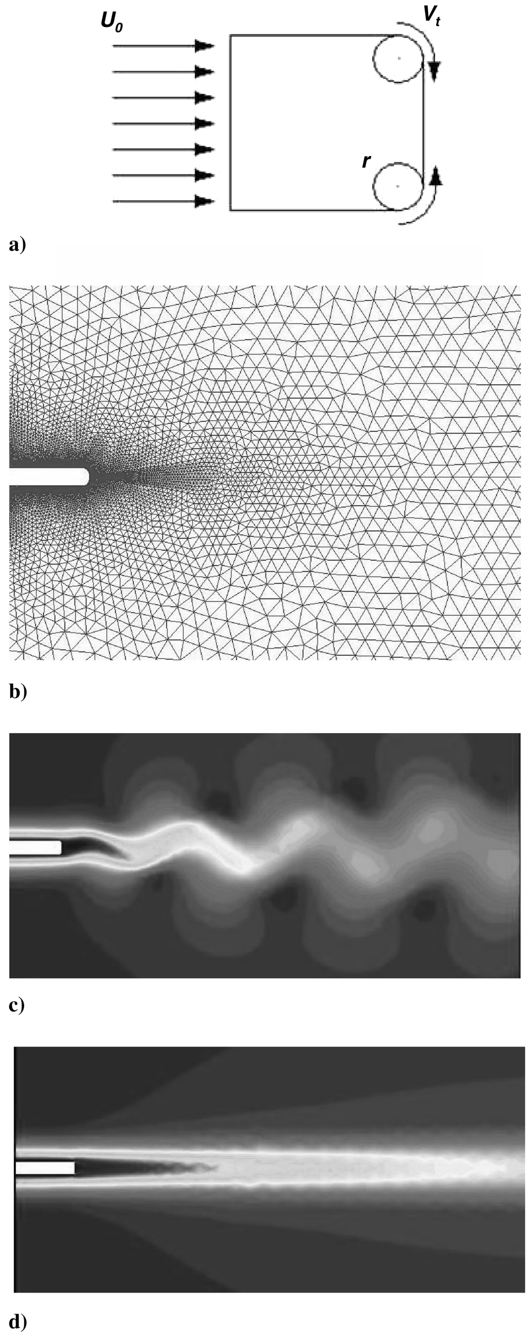

Fig. 4 a) Definition of parameters in the bluff-body model. b) Mesh used in a rectangular body configuration. c) Basic flow velocity component $\bar{u}$ obtained at $Re = 200, A_r = 0$. d) Same at $A_r = 0.1$.

B. Instability Analyses

1. Rectangular Duct Flow

From a numerical point of view, the EVP to be solved in the presence of $\bar{w} \neq 0$ is complex, and no reduction to a real problem is possible. Consequently, conclusions on the performance of the finite element method reached on this problem will carry weight in the solution of the more straightforward real eigenvalue problems that follow.

First, a square duct at low Reynolds number value, $Re = 100$, is considered, which is known to permit a relatively coarse resolution [36], such that numerical experimentation is straightforward. The complex EVP (36–39) is solved on $\mathcal{O}(10^4)$ nodes, requiring a very low tolerance in the solution of the linear systems, t-GMRES $= 10^{-20}$, and varying the Krylov subspace dimension, m; the results are presented in Table 3. Convergence of the leading eigenvalue is achieved at a moderate Krylov subspace dimension, $m = 20$, using a well-acceptable 600 Mb of in-core memory. The relative error of the eigenvalue obtained compared with the spectral collocation result [36] of the same complex EVP is on $\mathcal{O}(10^{-6})$.

The CPU time required for the solution of the EVP scales linearly with the Krylov subspace dimension m, and it is next interesting to identify the upper limit of the newly introduced parameter t-GMRES for convergence. Keeping $m = 20$ at the value previously obtained, results are presented in Table 4. It can be seen that values of $10^{-6} \leq t\text{-GMRES} \leq 10^{-5}$ are sufficient to ensure convergence at this Reynolds number value. At this combination of parameters, it is worth noticing that the computing cost of the present finite element methodology is already larger than that of a spectral solution of the complex EVP, the latter numerical methodology being ideally suited for the solution of the stability problem in the regular geometry at hand.

The situation as far as the efficiency of the numerical approach is concerned changes as the Reynolds number increases. It is known that increasingly larger grids will be necessary to resolve the increasingly finer structures appearing as the Reynolds number increases. The results of numerical experimentation with three meshes of different density at three Reynolds number values, $Re = 10^2$, 10^3, and 10^4, are shown in Table 5. All three meshes are capable of delivering the eigenvalue result at the lowest Reynolds number value. However, the highest-density mesh is necessary already at $Re = 10^3$; convergence is not achieved on any of the three meshes at the highest Reynolds number value, $Re = 10^4$. Actually even the sign of the leading eigenmode is wrong in the latter case: it is well known that the square duct flow is stable at all Reynolds numbers [15]. Also worth noting is that, on account of the increase of the (serial) computational time as the Reynolds number increases, it becomes increasingly inefficient to attempt a solution of the complex BiGlobal EVP at Reynolds numbers beyond $Re = \mathcal{O}(10^3)$. This is to be expected, given the low formal order of accuracy of the method.

Table 3 Dependence of the leading eigenvalue on the Krylov subspace dimension m, at $Re = 100$, for a grid comprising 11,605 nodes and a tolerance in the solution of the linear system, t-GMRES = 1e-20

m	CPU time, min	Memory, Mb	ω_r	ω_i
10	9	644	−0.139615	0.590645
15	13	644	−0.140494	0.594231
20	17	645	−0.140503	0.594177
60	49	702	−0.140503	0.594177

Table 4 Dependence of the leading eigenvalue on the tolerance in the solution of the linear system, t-GMRES, at $Re = 100$, for a grid comprising 11,605 nodes and a Krylov subspace dimension $m = 20$

log(t-GMRES)	CPU time, s	Memory, Mb	ω_r	ω_i
−3	116	621	−0.140552	0.594184
−4	124	621	−0.140482	0.594169
−5	132	622	−0.140502	0.594178
−7	144	622	−0.140503	0.594178
−10	555	644	−0.140503	0.594177
−14	583	645	−0.140503	0.594177
−20	1013	645	−0.140503	0.594177

Table 5 Grid dependence of eigenvalue results in square duct flow. Parameters used are as follows: ILU preconditioner tolerance: t-ILU = 5.0e-4; $\beta = 1$; Krylov subspace dimension $m = 60$; solution tolerance: t-GMRES = 1e-20

Nodes	Memory, Mb	Time, min	ω_r	ω_i
$Re = 100$				
5129	680	17	−0.140498	0.594178
11,605	702	49	−0.140503	0.594177
60,465	1950	280	−0.140507	0.594177
$Re = 1000$				
5129	648	13	−0.078650	0.868472
11,605	642	43	−0.072671	0.862796
60,465	2037	442	−0.070679	0.865575
$Re = 10,000$				
5129	615	8	0.004313	0.729155
11,605	535	327	0.002169	0.765670
60,465	2000	254	0.004469	0.766477

Table 6 Critical parameter (Re, β) values of the four most significant modes as a function of duct aspect ratio [36]; $m = 40$, t-GMRES = 1.0e-16

AR	Re	β	Nodes	ω_i
3.5	36,600	0.71	13,279	0.121660885
4	18,400	0.80	29,725	0.161186414
5	10,400	0.91	57,657	0.210532778

On the other hand, computational efficiency considerations aside, once sufficient resolution is provided, the method is capable of providing results in very good agreement with the established spectral computations. The predictions of the leading eigenmode frequency at critical conditions as function of the duct aspect ratio are shown in Table 6, in which the relative error in this quantity, compared with the spectral computations of Theofilis et al. [36], can be seen to vary between 4×10^{-3} at the lower two Reynolds numbers and 1.5×10^{-2} at the highest Reynolds number value. The eigenfunctions pertinent to the least-damped mode at $(Re, \beta) = (100, 1)$ at AR $= 3.5$ are presented in Fig. 5.

The conclusion at which one arrives on the basis of the numerical experimentation presented is that the suite of finite-element-based algorithms exposed presented is capable of delivering accurate predictions for the complex BiGlobal EVP at Reynolds numbers of typical relevance to instability analysis. However, the efficiency of the iterative methods for the (serial) solution of the linear systems within the Arnoldi step deteriorates with increasing Reynolds number. On the other hand, the real EVP (also addressed in previous finite-element-based BiGlobal analyses) requires the manipulation of arrays whose size is approximately half that of those corresponding to the complex EVP. The ability to solve the latter problem is thus sufficient indication for the capacity of the finite element algorithms presented to solve the real EVP as well; the numerical experimentation with the complex EVP also serves as indication on the computational effort required for the solution of the real EVP, to which we turn next.

2. Rectangular Regularized Lid-Driven Cavity

The instability problem in the regularized rectangular lid-driven cavity has been solved employing both the LNSE and the EVP methodologies, respectively, based on numerical solution of (16), (17), and (44). In addition, a spectral collocation algorithm [31,36] has been used for comparisons. Attention is first focused on the stable test case $(Re, \beta) = (200, 2)$. The grid used for the basic flow calculations, comprising $\mathcal{O}(2 \times 10^4)$ (quadratic) velocity nodes, has been used for the instability analyses. Results are presented in

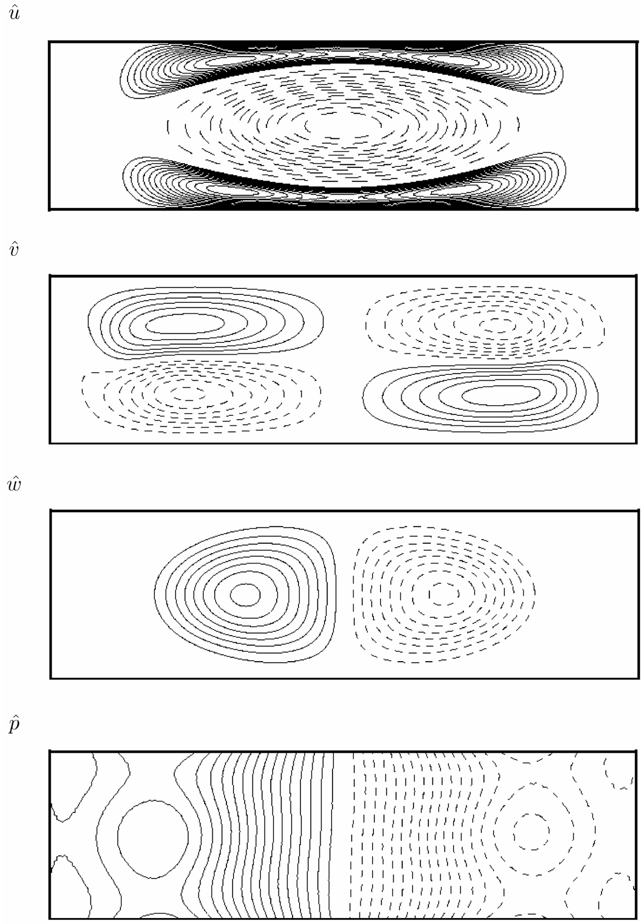

Fig. 5 Eigenfunctions pertaining to the leading eigenmode of AR $= 3.5$ rectangular duct flow at $Re = 100$, $\beta = 1.0$.

Table 7, in which a good agreement between the results of the three independent methodologies may be seen. The origin of the discrepancies between the results obtained by the LNSE and the EVP finite element methodologies on the one hand and the spectral method on the other is to be traced in the degree of spatial convergence of the basic state computed by the finite element approach and the relatively low Krylov subspace dimension, $m = 20$, used in the finite element computations. On the other hand, the differences in the results of the two finite element methodologies originate in the second-order approximation of the time derivative of the LNSE signal, from which the frequency and damping rate results are computed.

Interestingly, at this Reynolds number the regularization condition (59) results in a general stabilization of the global eigenmodes, especially at large β values, when compared with the standard lid-driven cavity (LDC) flow, in which the singular boundary condition $\bar{u}(x, y = 1) = 1$ is used in the place of (59). This result is in line with the analogous prediction of Theofilis [31], who analyzed a family of regularized profiles of the class discussed here. In addition, the frequency of the leading eigenmode is lower in the regularized compared with the singular lid-driven cavity configuration; both results are depicted in Fig. 6. The spatial distribution of the amplitude functions are qualitatively analogous; that of the leading eigenmode in the regularized LDC flow at $(Re, \beta) = (200, 2)$ is shown in Fig. 7.

Table 7 Dependence of the least-stable eigenmode at $Re = 200$ in the regularized square lid-driven cavity on the spanwise wave number β, as obtained by the finite-element (FE)-based LNSE and EVP-fe methodologies and comparison with the spectral-collocation (SC)-based EVP-SC approach

LNSE			EVP-FE		EVP-SC	
β	ω_r	$\pm\omega_i$	ω_r	$\pm\omega_i$	ω_r	$\pm\omega_i$
1	−0.3087	0.0000	−0.3092	0.0000	−0.3091	0.0000
2	−0.2459	0.0000	−0.2442	0.0000	−0.2437	0.0000
3	−0.2946	0.0786	−0.2913	0.0791	−0.2914	0.0788
4	−0.3077	0.2047	−0.3063	0.2051	−0.3059	0.2056
5	−0.3550	0.3147	−0.3531	0.3145	−0.3524	0.3153
6	−0.4155	0.4166	−0.4150	0.4154	−0.4140	0.4161
7	−0.4822	0.5083	−0.4839	0.5056	−0.4828	0.5060
8	−0.5494	0.5796	−0.5521	0.5799	−0.5512	0.5803
9	−0.6303	0.6359	−0.6317	0.6326	−0.6308	0.6323

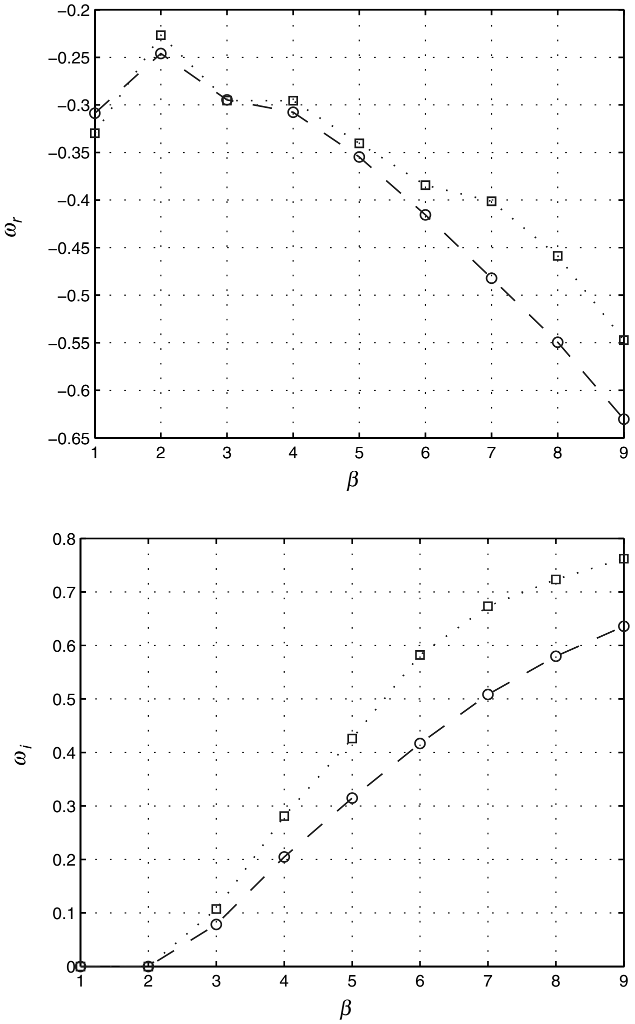

Fig. 6 Comparison of the dependence of ω_r (upper) and ω_i (lower) on β, as obtained in the singular [31] (squares) and regularized (circles) lid-driven cavity at $Re = 200$.

A consequence of the difference in amplification/damping rates between the two cavity configurations is the increase of the linear critical Reynolds number pertinent to all known modes of the singular lid-driven cavity, S1, T1, T2, and T3 [31]. In particular, the least-stable stationary mode S1 of the regularized LDC flow is now substantially more stable than that of its singular counterpart, such that the first unstable mode is of traveling nature. The dependence of the amplification rate of this mode, T1, on the spanwise wave number β is shown in Fig. 8. Finally, the effect of the aspect ratio on the instability of the regularized LDC has been examined. Four cases have been considered, AR $= 0.5$, 1, 2, and 4, to be able to draw qualitative conclusions on the effect of AR on the stability of the 3-D flow. The results are shown in graphical form in Fig. 9, whereas the critical parameter values may be found in Table 8.

3. *Triangular Regularized Lid-Driven Cavity*

By contrast to the previous regular geometries, which may also be resolved (more efficiently) by structured meshes, and have received

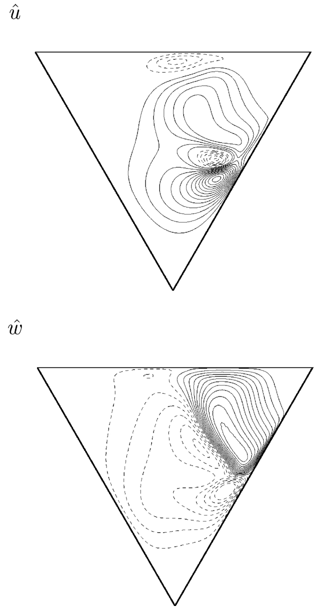

Fig. 7 Normalized eigenvectors in the rectangular regularized lid-driven cavity, pertaining to the least-damped eigenmode at $(Re, \beta) = (200, 2)$.

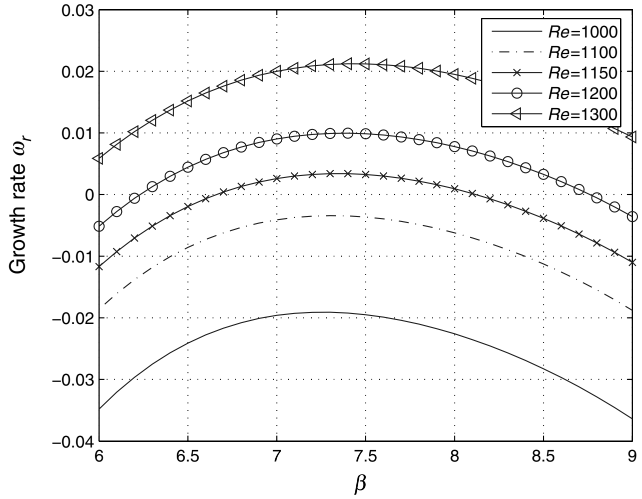

Fig. 8 Dependence of the growth rate ω_r on β at different Reynolds numbers around the critical conditions of mode T1.

attention as regards both their basic flow and their linear instability, the triangular cavity flow has been substantially less investigated, and only from a basic flow point of view. However, it is clear that should a linear instability be present in the triangular cavity, the corresponding critical Reynolds number will define the upper limit beyond which 2-D numerical solutions of the basic flow problem will only be of academic value.

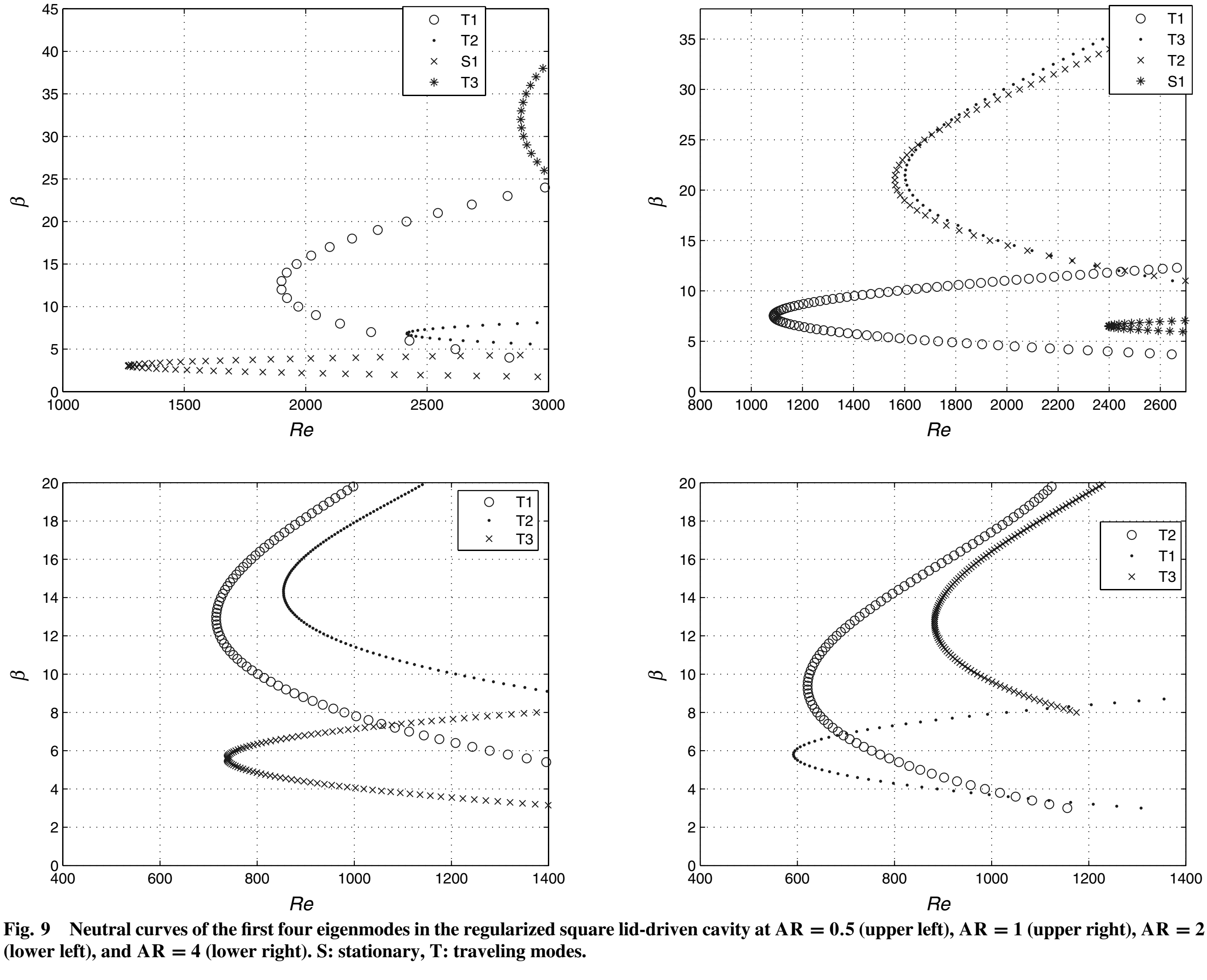

Fig. 9 Neutral curves of the first four eigenmodes in the regularized square lid-driven cavity at AR = 0.5 (upper left), AR = 1 (upper right), AR = 2 (lower left), and AR = 4 (lower right). S: stationary, T: traveling modes.

Table 8 Rectangular regularized LDC flow: critical parameter (Re, β, ω_i) values of the four most significant modes as a function of cavity aspect ratio; an asterisk denotes that this mode does not appear in the parameter range examined, $Re \in [0, 3000] \times \beta \in [0, 45]$

AR	S1	T1	T2	T3
0.5	(1268.7,3.05,0)	(1900.3, 12.0, 0.84)	(2417.1, 6.8, 0.47)	(2885.7, 32.0, 0.46)
1.0	(2397.7,6.5,0)	(1087.4, 7.5, 0.57)	(1561.0, 21.0, 0.16)	(1601.5, 21.5, 0.36)
2.0	*	(687.8, 5.6, 0.41)	(810.9, 13.6, 0.22)	(918.5, 19.0, 0.67)
4.0	*	(591.9, 5.8, 0.41)	(621.1, 9.4, 0.15)	(882.3, 12.7, 0.51)

High-resolution basic flows were obtained, in view of the a priori unknown resolution requirements for the solution of the real EVP (44) on which the present analyses have been based. However, the finely resolved basic states would result in prohibitively large memory requirements for the instability analysis, such that the basic flow results were interpolated from the finest to coarser grids, and the instability analysis results were monitored for convergence. Resolutions comprising up to $\mathcal{O}(2 \times 10^4)$ nodes were found to be adequate to provide reliable amplification rate information.

Steady basic flows in the Reynolds number range $Re \in [0, 5000]$ took increasingly long times to converge as the highest Reynolds number value examined was approached, which was taken as indication of linear amplification of the $\beta = 0$ eigenmode. The homogeneous spanwise direction $\beta \in [0, 30]$ was then examined at regular intervals of Reynolds number within the aforementioned range and the dependence of the amplification rate of a single unstable mode discovered on β, in the neighborhood of the critical conditions, is shown in Fig. 10a. A zero-crossing has been found to occur at the (near-) critical parameters

$$(Re, \beta) \approx (1870, 6.73) \tag{61}$$

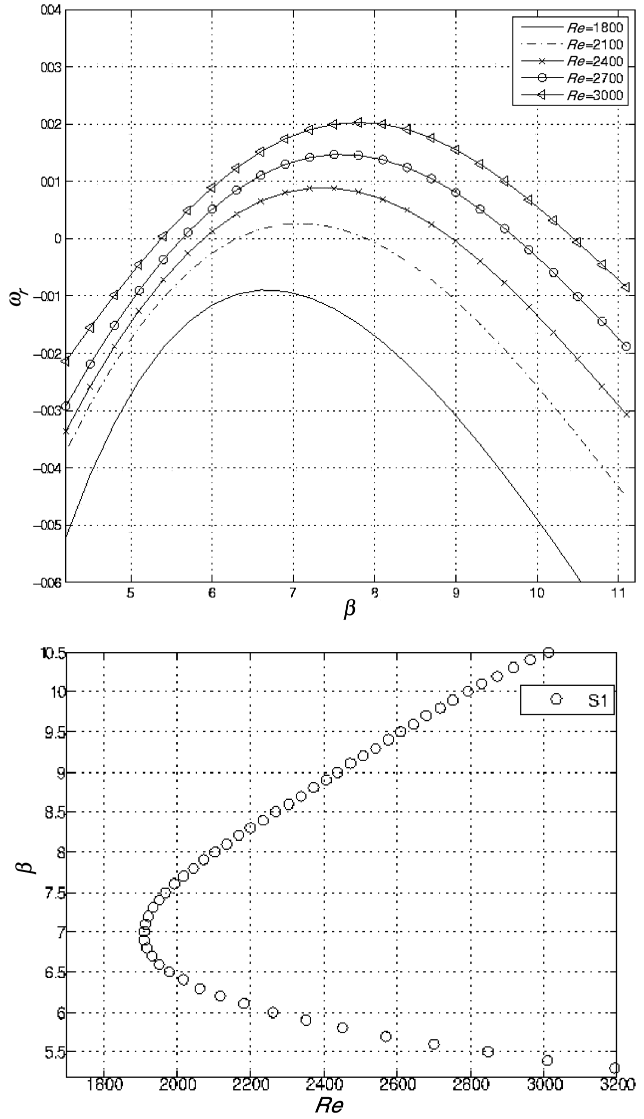

Fig. 10 a) Dependence of the amplification rate of the triangular cavity on β, in the neighborhood of the critical conditions. b) Neutral loop pertaining to the leading stationary unstable 3-D eigenmode.

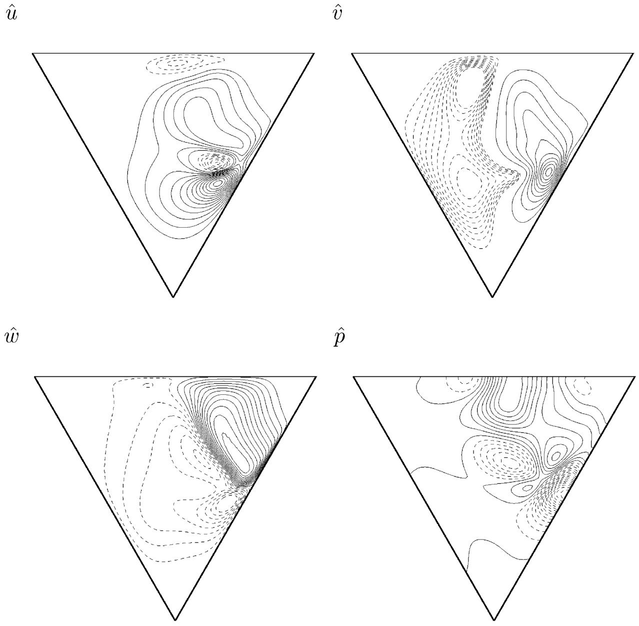

Fig. 11 Normalized eigenvectors in the triangular regularized lid-driven cavity, pertaining to the (near-) critical eigenmode (Re, β) = (1870, 6.73).

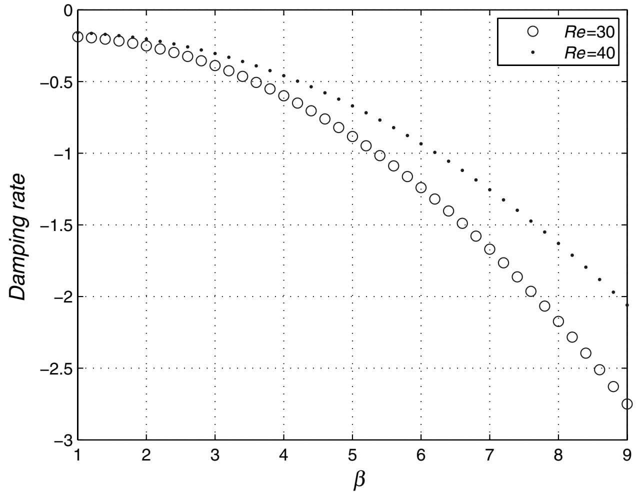

Fig. 12 Dependence of the damping rate ω_r on the spanwise wave number β in the bluff-body model.

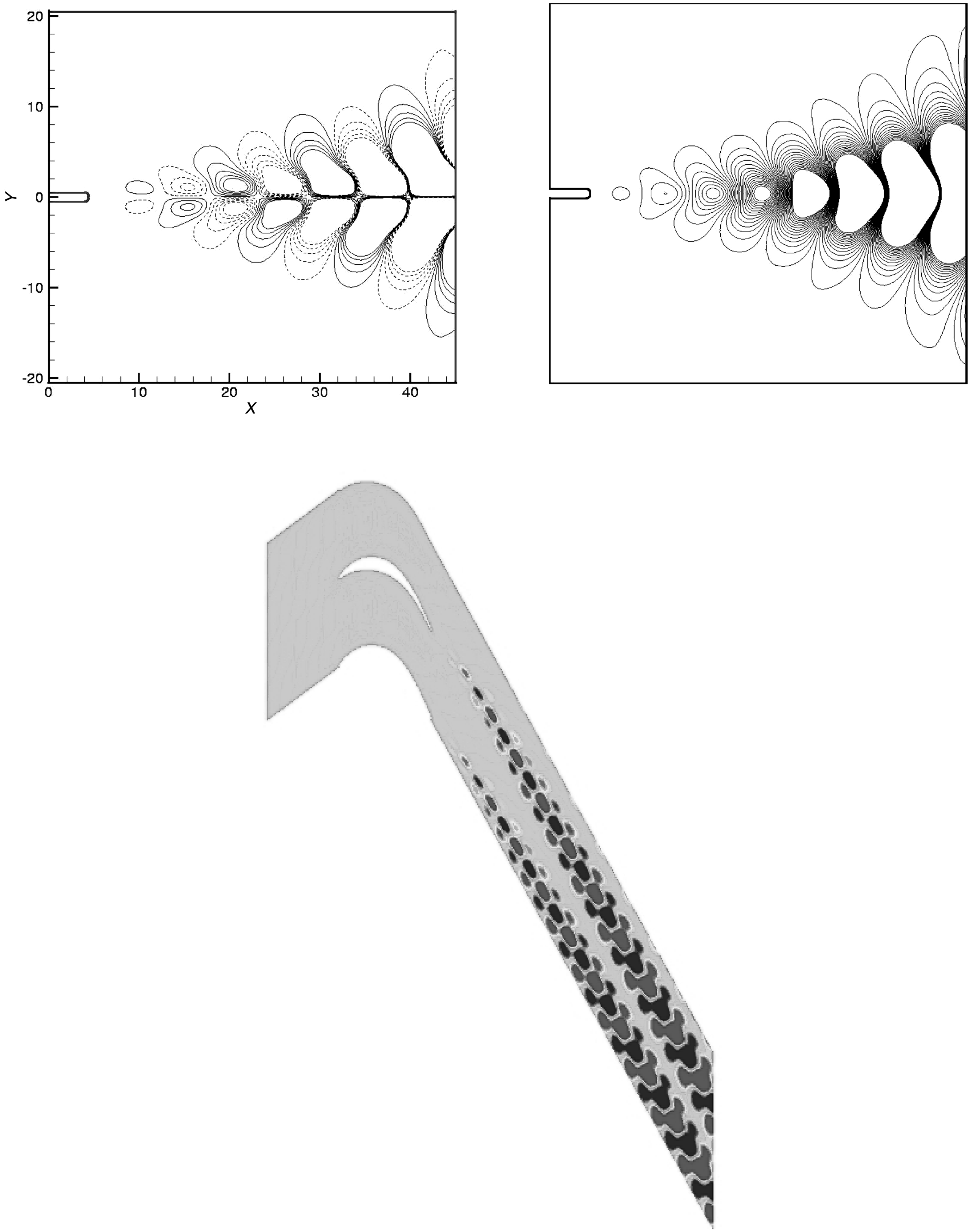

Fig. 13 Streamwise $\bar{u}$ (upper left) and normal $\bar{v}$ (upper right) amplitude functions of the leading eigenmode at *Re* = 30, $\beta = 2$. For comparison the corresponding result at *Re* = 893, $\beta = 0$ of a periodic row of low-pressure turbine blades [19] is shown.

Interpolation between the available instability results has delivered the neutral loop, presented in Fig. 10b. The neutral-loop results (of which only those in the neighborhood of the critical conditions are presented) confirm the tendency of the flow to become linearly unstable against the 2-D BiGlobal eigenmode $\beta = 0$ as the Reynolds number increases, and also explain the consequent increasing difficulties to obtain a stationary solution in this range.

The linearly unstable mode discovered is stationary; the amplitude functions of its components have been found to comprise only real parts, shown in Fig. 11. In contrast to the rectangular cavity examined earlier, within the parameter range examined, no traveling (or other stationary) modes have been found in the triangular cavity.

4. *Instability in the Wake of a Model Bluff Body*

As mentioned, this problem is an open system and, as such, offers the possibility to assess the performance of the numerical algorithms verified in the previous three flows in closed domains. Linear instability analyses in the model bluff body have been performed on the basis of (16), (17), and (44). In both the LNSE- and the EVP-based instability analyses, no-slip condition has been imposed at the surface of the bluff body Γ_b, alongside zero disturbance velocity at the inflow, upper, and lower domain boundaries $\Gamma_{\text{in}} \bigcup \Gamma_{\text{tb}}$ and natural boundary conditions for the outflow boundary Γ_{out}. The initial condition used for the LNSE was $(\hat{u}, \hat{v}) = (1, 0)$ at Γ_{in}. Preliminary results on the basis of the LNSE equations have been presented elsewhere [9].

Three-dimensional BiGlobal instability analysis of steady basic flows at subcritical Reynolds numbers has revealed that the 2-D flow is less stable than its 3-D counterparts. Results on the dependence of the damping rate of 3-D disturbances on β at two subcritical Reynolds numbers are shown in Fig. 12. The 2-D flow is found to be least stable, a result which is in line with the prediction of Squire's theorem, should one choose to address the stability of this wake as a problem based on the (1-D) Orr–Sommerfeld equation. This result is qualitatively analogous with that in both the circular cylinder [16] and the T-106/300 low-pressure turbine (LPT) flow [12,19]. A key difference with the latter work, besides the high-order spectral/*hp* element method used in the LPT studies, is the imposition of periodic boundary conditions (corresponding to a cascade of rows) on the upper and lower domain boundaries of the LPT flowfield. By contrast, in the present model, the flow is permitted to develop over a wider domain, which results in destabilization of the flow. The effect of the boundary conditions on the development of the eigenfunctions may be appreciated by comparing results of the two applications. The amplitude functions pertaining to the streamwise $\hat{u}$ and normal $\hat{v}$ disturbance velocity components of the least-stable eigenmode at $(Re, \beta) = (30, 2)$ are shown in Fig. 13. Because of the definition of the Reynolds number on the chord length in the LPT application, a concept inapplicable in the model bluff body, one-to-one comparisons are not possible. Nevertheless, the analogy of the results in the two applications, as well as the physically consistent picture emerging as regards instability of bluff bodies, and models thereof, permits asserting that the present suite of numerical algorithms is well capable of answering the question regarding the physical mechanism underlying the wake stabilization approach of Patnaik and Wei [32]. Work on this topic is currently underway and results will be presented elsewhere.

IV. Conclusions

A suite of numerical algorithms for the computation of BiGlobal linear instability of flows in complex domains has been presented. Spatial discretization is based on a Taylor–Hood finite element approach, using space tessellation on unstructured meshes. Temporal discretization of the equations has been considered both within a linearized Navier–Stokes context, as well as through solution of the eigenvalue problem. A novelty of the present work compared with analogous earlier analyses has been the demonstration of its ability to solve the complex EVP, albeit at a cost which may, at large Reynolds numbers of $\mathcal{O}(10^4)$, become prohibitively high for serial computations. On the other hand, the real EVP has been found to be well-tractable at all Reynolds number examined.

As demonstrators of the proposed numerical methods, four problems of varying degree of complexity have been presented. The rectangular duct flow has been revisited, because it represents a prototype instability problem based on the complex EVP. On the other hand, the instability of the other three problems has been addressed on the basis of the real BiGlobal (LNSE- and/or EVP-based) equations. Results in the rectangular regularized lid-driven cavity flow complement earlier works on the classic counterpart of this flow in which singular boundary conditions are imposed. Regularization was found to have a stabilizing effect. Conversely, an increasing aspect ratio results in progressive destabilization of the flow, in line with the analogous finding in the singular lid-driven cavity. Both stationary and traveling BiGlobal eigenmodes have been identified and the critical conditions for four cavity geometries have been documented. The regularized lid-driven cavity of equilateral triangular shape has also been analyzed for the first time. It has been demonstrated that beyond a Reynolds number of $\mathcal{O}(2 \times 10^4)$ (presently unavailable) 3-D solutions of the equations of motion should yield different predictions than those based on the 2-D equations, on account of linear amplification of a 3-D BiGlobal mode. The latter has been identified herein to have a periodicity length of approximately that of the triangle side. Finally, instability in the wake of a model bluff body was analyzed, delivering predictions in line with those of known bluff-body flows as regards the destabilization of the 2-D flow, before the (potential) onset of three-dimensionality. Here, the numerical tools developed permit analyzing the origins of the stabilization of the wake by means of modifications of the wall boundary conditions. The development of a finite-element-based Floquet instability analysis, along the lines of existing spectrally accurate tools for the cylinder [16] and the low-pressure turbine [12], as well as work on parallelization of the algorithms presented herein, are the principal lines along which future work is envisaged.

Appendix: Details of the Variational Formulation

Defining the quadratic velocity basis functions as ψ and the linear pressure basis functions as ϕ, the following entries of the matrices A and B of the generalized BiGlobal EVP appearing in Eq. (44) are obtained:

$$\gamma_{ij} = \bar{u}_m^l \int_\Omega \psi_l \frac{\partial \psi_i}{\partial x_m} \psi_j \,\mathrm{d}\Omega, \qquad l, i, j = 1, \ldots, N \tag{A1}$$

$$C_{ij}^{mk} = \left(\frac{\partial \bar{u}_m}{\partial x_k}\right)^l \int_\Omega \psi_l \psi_i \psi_j \,\mathrm{d}\Omega, \qquad l, i, j = 1, \ldots, N \qquad m = 1, 2, 3 \qquad k = 1, 2 \tag{A2}$$

$$E_{ij} = \bar{u}_3^l \int_\Omega \psi_l \psi_i \psi_j \,\mathrm{d}\Omega, \qquad l, i, j = 1, \ldots, N \tag{A3}$$

$$R_{ij} = \int_\Omega \frac{\partial \psi_i}{\partial x_m} \frac{\partial \psi_j}{\partial x_m} \,\mathrm{d}\Omega, \qquad i, j = 1, \ldots, N \qquad m = 1, 2 \tag{A4}$$

$$M_{ij} = \int_\Omega \psi_i \psi_j \,\mathrm{d}\Omega, \qquad i, j = 1, \ldots, N \tag{A5}$$

$$D_{ij} = \int_\Omega \phi_i \psi_j \,\mathrm{d}\Omega, \qquad i = 1, \ldots, \mathrm{NL} \qquad j = 1, \ldots, N \tag{A6}$$

$$\lambda_{ij}^x = \int_\Omega \phi_i \frac{\partial \psi_j}{\partial x}, \qquad i = 1, \ldots, \mathrm{NL} \qquad j = 1, \ldots, N \,\mathrm{d}\Omega \tag{A7}$$

$$\lambda_{ij}^y = \int_\Omega \phi_i \frac{\partial \psi_j}{\partial y}, \qquad i = 1, \ldots, \mathrm{NL} \qquad j = 1, \ldots, N \,\mathrm{d}\Omega \tag{A8}$$

References

[1] Drazin, P. G., and Reid, W. H., *Hydrodynamic Stability*, Cambridge Univ. Press, Cambridge, England, 1981.

[2] Schmid, P., and Henningson, D. S., *Stability and Transition in Shear Flows*, Springer, New York, 2001.

[3] Theofilis, V., "Advances in Global Linear Instability Analysis of Nonparallel and Three-Dimensional Flows," *Progress in Aeronautical Sciences*, Vol. 39, No. 4, 2003, pp. 249–315.

[4] Luijkx, J. M., and Platten, J. K., "On the Onset of Free Convection in a Rectangular Channel," *Journal of Non-Equilibrium Thermodynamics*, Vol. 6, 1981, pp. 141–158.

[5] Jackson, C. P., "A Finite-Element Study of the Onset of Vortex Shedding in Flow Past Variously Shaped Bodies," *Journal of Fluid Mechanics*, Vol. 182, Sept. 1987, pp. 23–45.

[6] Zebib, A., "Stability of Viscous Flow Past a Circular Cylinder," *Journal of Engineering Mathematics*, Vol. 21, No. 2, June 1987, pp. 155–165.

[7] Morzynksi, M., and Thiele, F., "Numerical Stability Analysis of Flow About a Cylinder," *Zeitschrift fuer Angewandte Mathematik und Mechanik*, Vol. 71, No. 4, 1991, pp. T242–T248.

[8] Ehrenstein, U., and Gallaire, F. P., "On Two-Dimensional Temporal Modes in Spatially Evolving Open Flows: The Flat Plate Boundary Layer," *Journal of Fluid Mechanics*, Vol. 536, Aug. 2005, pp. 209–218.

[9] Simens, M., González, L., Theofilis, V., and Gómez-Blanco, R., "On Fundamental Instability Mechanisms of Nominally 2D Separation Bubbles," *Sixth IUTAM Symposium on Laminar-Turbulent Transition*, edited by R. Govindarajan, Springer, New York, 2006, pp. 89–95.

[10] Gelfgat, A. Y., "Different Modes of Rayleigh-Bénard Instability in Two- and Three-Dimensional Rectangular Enclosures," *Journal of Computational Physics*, Vol. 156, Dec. 1999, pp. 300–324.

[11] Leriche, E., and Labrosse, G., "Vector Potential-Vorticity Relationship for the Stokes Flows: Application to the Stokes Eigenmodes in 2D/3D Closed Domain," *Theoretical and Computational Fluid Dynamics*, Vol. 21, No. 1, Jan. 2007, pp. 1–13

[12] Abdessemed, N., Sherwin, S. J., and Theofilis, V., "Linear Stability of the Flow Past a Low Pressure Turbine Blade," AIAA Paper 2006-3530, 2006.

[13] Delbende, I., Chomaz, J.-M., and Huerre, P., "Absolute and Convective Instabilities in the Batchelor Vortex: A Numerical Study of the Linear Impulse Response," *Journal of Fluid Mechanics*, Vol. 485, Jan. 1998, pp. 221–242.

[14] Li, Y. S., and Kot, S. C., "One-Dimensional Finite Element Method in Hydrodynamic Stability," *International Journal of Numerical Methods in Engineering*, Vol. 17, No. 6, 1981, p. 853.

[15] Tatsumi, T., and Yoshimura, T., "Stability of the Laminar Flow in a Rectangular Duct," *Journal of Fluid Mechanics*, Vol. 212, March 1990, pp. 437–449.

[16] Barkley, D., and Henderson, R. D., "Three-Dimensional Floquet Stability Analysis of the Wake of a Circular Cylinder," *Journal of Fluid Mechanics*, Vol. 322, Sept. 1996, pp. 215–241.

[17] Karniadakis, G. E., and Sherwin, S. J., *Spectral/hp Element Methods for Computational Fluid Dynamics*, 2nd ed., Oxford Univ. Press, Oxford, 2005.

[18] Theofilis, V., Barkley, D., and Sherwin, S. J., "Spectral/hp Element Technology for Flow Instability and Control," *The Aeronautical Journal*, Vol. 106, No. 1065, 2002, pp. 619–625.

[19] Abdessemed, N., Sherwin, S. J., and Theofilis, V., "On Unstable 2D Basic States in Low Pressure Turbine Flows at Moderate Reynolds Numbers," AIAA Paper 2004-2541, 2004.

[20] Sherwin, S. J., and Blackburn, H. M., "Three-Dimensional Instabilities of Steady and Pulsatile Axisymmetric Stenotic Flows," *Journal of Fluid Mechanics*, Vol. 533, June 2005, pp. 297–327.

[21] Fietier, N., and Deville, M., "Time-Dependent Algorithms for the Simulation of Viscoelastic Flows with Spectral Element Methods: Applications and Stability," *Journal of Computational Physics*, Vol. 186, No. 1, 2003, pp. 93–121.

[22] Strykowski, P. J., and Sreenivasan, K. R., "On the Formation and Suppression of Vortex "Shedding" at Low Reynolds Numbers," *Journal of Fluid Mechanics*, Vol. 218, Sept. 1990, pp. 71–107.

[23] Noack, B., Tadmor, G., and Morzynski, M., "Low-Dimensional Models for Feedback Flow Control. Part 1: Empirical Galerkin Models," AIAA Paper 2004-2408, 2004.

[24] Ding, Y., and Kawahara, M., "Linear Stability of Incompressible Flow Using a Mixed Finite Element Method," *Journal of Computational Physics*, Vol. 139, No. 2, Jan. 1998, pp. 243–273.

[25] Ding, Y., and Kawahara, M., "Three-Dimensional Linear Stability Analysis of Incompressible Viscous Flow Using the Finite Element Method," *International Journal for Numerical Methods in Fluids*, Vol. 31, No. 2, 1999, pp. 451–479.

[26] Bourcier, M., and Francois, C., "Integration Numerique des Equations de Navier-Stokes dans un Domine Carré," *La Recherché Aerospatiale*, Vol. 131, July–Aug. 1969, pp. 23–33.

[27] Cuvelier, C., Segal, A., and van Steenhoven, A. A., *Finite Element Methods and Navier-Stokes Equations*, D. Reidel Publishing Company, Dordrecht, The Netherlands, 1986.

[28] Allievi, A., and Bermejo, R., "A Characteristic-Finite Element Conjugate Gradient Algorithm for the Navier-Stokes Equations," *International Journal for Numerical Methods in Fluids*, Vol. 32, No. 4, 2000, pp. 439–463.

[29] Clie, K. A., Garratt, T. J., and Spence, A., *SIAM Journal on Matrix Analysis and Applications*, Vol. 15, No. 4, 1994, p. 1310.

[30] Meerbergen, K., Spence, A., and Rose, D., *BIT*, Vol. 34, No. 3, 1994, p. 409.

[31] Theofilis, V., "Globally Unstable Basic Flows in Open Cavities," AIAA Paper 2000-1965, 2000.

[32] Patnaik, B. S. V., and Wei, G. W., "Controlling Wake Turbulence," *Physical Review Letters*, Vol. 88, Jan. 2002, pp. 054502-1–4.

[33] González, L. M., and Bermejo, R., "A Semi-Langrangian Level Set Method for Incompressible Navier-Stokes Equations with Free Surface," *International Journal for Numerical Methods in Fluids*, Vol. 49, No. 10, Dec.–2005, pp. 1111–1146.

[34] Dean, E. J., and Glowinski, R., *Incompressible Computational Fluid Dynamics*, Cambridge Univ. Press, Cambridge, England, 1993, pp. 109–150.

[35] Meijerink, J., and van der Vorst, H., "An Iterative Solution Method for Linear Systems of Which the Coefficient Matrix is a Symmetric M-Matrix," *Mathematics of Computation*, Vol. 31, No. 137, 1977, pp. 148–162.

[36] Theofilis, V., Duck, P. W., and Owen, J., "Viscous Linear Stability Analysis of Rectangular Duct and Cavity Flows," *Journal of Fluid Mechanics*, Vol. 505, April 2004, pp. 249–286.

[37] Saad, Y., "SPARSKIT, a Basic Tool Kit for Sparse Matrix Computations," Univ. of Minnesota, Minneapolis, MN, http://www-users.cs.umn.edu/~saad/software/SPARSKIT/sparskit.html [retrieved 11 Jan._2007], 1994.

[38] Theofilis, V., "Linear Instability Analysis in Two Spatial Dimensions," *Proceedings of the 4th European Computational Fluid Dynamics Conference*, edited by K. D. Papailiou, Vol. 1, No. 1, ECCOMAS, Athens, 1998, pp. 547–552.

[39] Uhlmann, M., and Nagata, M., "Linear Stability of Flow in an Internally Heated Rectangular Duct," *Journal of Fluid Mechanics*, Vol. 551, March 2006, pp. 387–404.

[40] Leriche, E., Gavrilakis, S., and Deville, M. O., "Direct Simulation of the Lid-Driven Cavity Flow with Chebyshev Polynomials," *Proceedings of the 4th European Computational Fluid Dynamics Conference*, edited by K. D. Papailiou, Vol. 1, No. 1, ECCOMAS, Athens, 1998, pp. 220–225.

[41] Poliashenko, M., and Aidun, C. K., "A Direct Method for Computation of Simple Bifurcations," *Journal of Computational Physics*, Vol. 121, No. 2, Oct. 1995, pp. 246–260.

[42] Erturk, E., and Gokol, O., "Fine Grid Benchmark Solutions of Triangular Cavity Flow," *International Journal of Numerical Methods for Heat and Fluid Flow* (submitted for publication).

[43] Gaskell, P. H., Thompson, H. M., and Savage, M. D., "A finite element analysis of steady viscous ow in triangular cavities," *Proceedings of the Institution of Mechanical Engineers. Part C, Journal of Mechanical Engineering Science*, Vol. 213, No. 3, 1999, pp. 263–276.

[44] McQuain, W. D., Ribbens, C. J., Wang, C.-Y., and Watson, L. T., "Steady Viscous Flow in a Trapezoidal Cavity," *Computers and Fluids*, Vol. 23, No. 4, May 1994, pp. 613–626.

[45] Li, M., and Tang, T., "Steady Viscous Flow in a Triangular Cavity by Efficient Numerical Techniques," *Computers and Mathematics with Applications (1975-) / Computers & Mathematics with Applications*, Vol. 31, No. 10, May 1996, pp. 55–65.

A. Tumin
Associate Editor